

Gravitational waves and mass ejecta from binary neutron star mergers: Effect of the mass-ratio

Tim Dietrich¹, Maximiliano Ujevic², Wolfgang Tichy³, Sebastiano Bernuzzi⁴, and Bernd Brügmann⁵

¹ *Max-Planck-Institut für Gravitations Physics, Albert-Einstein-Institut, D-14476 Golm, Germany*

² *Centro de Ciências Naturais e Humanas, Universidade Federal do ABC, 09210-170, Santo André, São Paulo, Brazil*

³ *Department of Physics, Florida Atlantic University, Boca Raton, FL 33431 USA*

⁴ *DiFeST, University of Parma, and INFN Parma I-43124 Parma, Italy and*

⁵ *Theoretical Physics Institute, University of Jena, 07743 Jena, Germany*

(Dated: July 25, 2016)

We present new (3+1)D numerical relativity simulations of the binary neutron star (BNS) merger and postmerger phase. We focus on a previously inaccessible region of the binary parameter space spanning the binary's mass-ratio $q \sim 1.00 - 1.75$ for different total masses and equations of state, and up to $q \sim 2$ for a stiff BNS system. We study the mass-ratio effect on the gravitational waves (GWs) and on the possible electromagnetic emission associated to dynamical mass ejecta. We compute waveforms, spectra, and spectrograms of the GW strain including all the multipoles up to $l = 4$. The mass-ratio has a specific imprint on the GW multipoles in the late-inspiral-merger signal, and it affects qualitatively the spectra of the merger remnant. The multipole effect is also studied by considering the dependency of the GW spectrograms on the source's sky location. Unequal mass BNSs produce more ejecta than equal mass systems with ejecta masses and kinetic energies depending almost linearly on q . We estimate luminosity peaks and light curves of macronovae events associated to the mergers using a simple approach. For $q \sim 2$ the luminosity peak is delayed for several days and can be up to four times larger than for the $q = 1$ cases. The macronova emission associated with the $q \sim 2$ BNS is more persistent in time and could be observed for weeks instead of few days ($q = 1$) in the near infrared. Finally, we estimate the flux of possible radio flares produced by the interaction of relativistic outflows with the surrounding medium. Also in this case a large q can significantly enhance the emission and delay the peak luminosity. Overall, our results indicate that BNS merger with large mass ratio have EM signatures distinct from the equal mass case and more similar to black hole - neutron star binaries.

PACS numbers: 04.25.D-, 04.30.Db, 95.30.Lz, 97.60.Jd 98.62.Mw

I. INTRODUCTION

Binary neutron star (BNS) mergers are primary sources of gravitational waves (GWs) and are associated with a variety of electromagnetic (EM) emissions. GW observations of BNS are eagerly expected in the upcoming LIGO-Virgo runs, after the first binary black hole (BBH) GW detections GW150914 [1] and GW151226 [2]. Such GWs will allow us to place constraints on the nature of matter at densities above nuclear density, e.g. [3], and to identify the origin of EM emissions like kilo/macronovae and short gamma-ray burst (SGRB), e.g. [4, 5]. Kilo/macronovae events are transient emissions in the optical or near-infrared band observed in e.g. [6]. They are believed to be triggered by the radioactive decay of r-process nuclei in the neutron-rich material ejected during a BNS merger. SGRBs models are instead based on highly relativistic outflows, powered e.g. by the merger remnant accretion disk [7, 8]. Their joint observation with GWs might be challenging due to the short duration of the burst and to the fact that they are highly collimated emissions [9]. Additionally, the interaction of mildly or sub-relativistic outflows with the surrounding material generates synchrotron radiation known as radio flares [10]. This emission can persist from months to years after merger, depending on the composition, which makes radio flares a particularly attractive EM counter-

part to detect.

Understanding the dependency of the GW and EM emissions on the source's parameters is of key importance for GW astronomy and multimessenger astrophysics. The BNS parameter space is composed by the component masses (and spins), and by a choice of equation of state (EOS) describing the NS matter. The ranges of the mass and spins parameters are rather uncertain.

The expected NS mass range is $\sim 0.9 - 3M_{\odot}$. The lower bound is inferred from the formation scenario (gravitational-collapse) and from current observations, although those measurements have typically large uncertainties, see e.g. [11, 12]. The upper bound is inferred from stability argument (maximum theoretical mass), from precise measurements of $\sim 2M_{\odot}$ NSs in double NS systems [13, 14], and from models of SGRBs, which suggest a maximum mass of $2.2M_{\odot}$, e.g. [15]. There exist observations of larger NS masses but with large uncertainties, so they cannot give strong constraints on the NS maximum mass [16]. Also, the maximum mass of a NS is determined by the particular EOS. Most tabulated EOS compatible with astrophysical constraints support NSs with maximum masses in a range of $\sim 2 - 3M_{\odot}$.

The above considerations suggest that the BNS mass-ratio

$$q := M^A/M^B \geq 1, \quad (1)$$

where $M^{A,B}$ are the individual gravitational masses of the NSs (in isolation), is most likely constrained to $q \lesssim 2 - 3$. Observations suggest that BNS systems consist of equal mass NSs with masses of around $\sim 1.35M_\odot$ and that the mass-ratio is close to one e.g. [16, 17]. However, only approximately a dozen BNS systems are known so far and only 6 of these systems have well determined masses and will merge within a Hubble time. The lack of very unequal mass configurations might only be a selection effect. For example Ref. [18] discovered a compact binary system with a mass ratio of $q \approx 1.3$, suggesting that BNS with larger mass ratios exist. Population synthesis models for binaries formed “*in situ*” predict a wider range of masses and mass ratios up to $q \approx 1.9$ [19, 20].

Also NS spins are constrained by theoretical arguments and observations, e.g. [20–23]. However, we do not consider here the NS rotation and we remind to the above references and to future work [24].

Parameter space investigation of BNS are challenging due to the unknown EOS, and the need of simulating each masses (and spins) configuration with different EOS. Most numerical relativity studies of BNS systems have focused on equal masses and irrotational configurations. The first simulations of unequal mass systems have been presented in [25–27] using polytropic and piecewise polytropic EOS. Mass ejecta in $q \neq 1$ BNS simulations have been studied in e.g. [27–29]. Unequal mass simulations with microphysical EOS and neutrino cooling have been presented in e.g. [30–32] and with radiation-hydrodynamics in [33]. Previous works were restricted to mass ratios $q \leq 1.35$. Overall, the main results are that i) asymmetric mergers produce more massive ejecta with smaller electron fractions than the corresponding equal mass setups ii) unequal mass systems are likely to produce kilonovae and iii) the remnant disk mass increases for an increasing mass ratio.

In [20] we reported an upgrade of the SGRID code able to generate generic initial data for BNS simulations together with few preliminary evolutions. Among other results, we showed the possibility of generating “large mass-ratio” configurations with $q \sim 2$. The test evolution of a $q = 2$ BNS showed interesting features, including large mass ejection and mass transfer from one star to the other during the last revolutions.

In this work we study the effect of the binary’s mass-ratio q on the GWs and on the characteristics of possible EM emission associated to dynamical mass ejecta, in particular macronovae and radio flares. We present a new set of (3+1)D numerical relativity simulations of the merger and postmerger phase, and focus on a previously inaccessible region of the binary parameter space spanning $q \in [1, 1.75]$ for different masses and equations of state, and a setup with $q = 2$.

The article is structured as follows: In Sec. II, we give a short description of the numerical methods and describe important quantities used to analyze our simulations. Section III summarizes our configurations and the

investigated part of the BNS parameter space. Section IV deals with the dynamics of the simulation, where in particular we focus on the mass-transfer, the ejecta, and the final remnant. The GW signal is investigated in Sec. V with respect to spectrograms, the sky location and the emitted GW energy per mode. Sec. VI focuses on EM counterparts and we conclude in Sec. VII. In Appendix A we test the accuracy of our simulations with respect to conserved quantities, convergence, the constraints.

Throughout this work we use geometric units, setting $c = G = M_\odot = 1$, though we will sometimes include M_\odot explicitly or quote values in CGS units for better understanding. Spatial indices are denoted by Latin letters running from 1 to 3 and Greek letters are used for spacetime indices running from 0 to 3.

II. SIMULATION METHODS

A. Initial configurations

Our initial configurations are constructed with the SGRID code [34–36]. SGRID uses pseudospectral methods to accurately compute spatial derivatives. To obtain stationary configurations that are appropriate as initial data, we use the conformal thin sandwich equations [37–39] together with assumptions of the constant rotational velocity approach [40, 41], which allows to construct generic NS binaries in hydrodynamical equilibrium. The computational domain is divided into six patches (Fig. 1 of [20]). The domain reaches spatial infinity and thus allows to impose exact boundary conditions at spatial infinity. Recent changes presented in [20] allow us to construct configurations in almost all corners of the BNS parameter space including high mass ratios, spinning configurations, low and high eccentricity inspirals, as well as more realistic EOSs and highly compact stars. In this work we do not study the influence of the eccentricity and spin, but focus on the high-mass ratio configuration and the influence of the EOS.

We employ $n_A = 28, n_B = 28, n_\varphi = 8, n_{\text{Cart}} = 24$ points for the spectral grid, cf. [20] for more details. In Tab. II we report the initial parameters, in particular, the initial ADM-mass and angular momentum of the system as well as the initial GW frequency.

B. Evolutions

Dynamical simulations are performed with the BAM code [29, 42, 43]. We use the Z4c scheme [44, 45] and employ the 1+log and gamma-driver conditions for the evolution of the lapse and shift [46–48].

The equations of general-relativistic hydrodynamics (GRHD) are solved in conservative form by defining Eulerian conservative variables from the rest-mass density ρ , pressure p , internal energy ϵ , and 3-velocity, v^i . The system is closed by an EOS. We model the EOS with piece-

wise polytropic fits of [49], see Tab. I below. Thermal effects are included during the simulation by an additive pressure contribution given by $p_{\text{th}} = (\Gamma_{\text{th}} - 1)\rho\epsilon$ [50, 51]. As in our previous work we set $\Gamma_{\text{th}} = 1.75$.

The evolution algorithm is based on the method-of-lines with explicit 4th order Runge-Kutta time integrators. Finite difference stencils of 4th order are employed for the spatial derivatives of the metric. GRHD is solved by means of a high-resolution-shock-capturing method [43] based on primitive reconstruction and the Local-Lax-Friedrichs (LLF) central scheme for the numerical fluxes. Primitive reconstruction is performed with the 5th order WENOZ scheme of [52]. We do not employ the higher-order algorithm presented recently in [53], because the new method was not tested at the time these simulations were performed.

The numerical domain is made of a hierarchy of cell-centered nested Cartesian grids. The hierarchy consists of L levels of refinement labeled by $l = 0, \dots, L - 1$. A refinement level l has one or more Cartesian grids with constant grid spacing h_l and n points per direction. The refinement factor is two such that $h_l = h_0/2^l$. The grids are properly nested, i.e., the coordinate extent of any grid at level l , $l > 0$, is completely covered by the grids at level $l - 1$. Some of the mesh refinement levels $l > l^{\text{mv}}$ can be dynamically moved and adapted during the time evolution according to the technique of “moving boxes”. The BAM grid setups considered in this work consist of 7 refinement levels. We distinguish between two different grid setups. For the first setup, we substitute the outermost level ($l = 0$) by a multipatch cubed-sphere grid [45, 54–56] on which we do not solve the GRHD equations. The spheres allow us to apply constraint preserving boundary conditions [57]. This ‘shell’ setup is denoted in Tab. II with the ending ‘s’. The second grid setup does not make use of the multipatch cubed-spheres, so all the refinement levels are Cartesian boxes. While this has the disadvantage that only Sommerfeld boundary conditions are used, it increases the computational speed and the matter fields are evolved on a larger region. We denote this ‘box’ setup by the ending ‘b’ in Tab. II.

The Berger-Oliger algorithm is employed for the time stepping [58] on the inner levels. As in [20, 29, 59] we make use of an additional refluxing algorithm to enforce mass conservation across mesh refinement boundaries based on [60, 61]. Restriction and prolongation between the refinement levels is performed with an average scheme and 2nd order essentially non-oscillatory scheme, respectively.

C. Simulation analysis

We briefly want to summarize important quantities for our simulation analysis. For this purpose we follow the description of [29] including also quantities to monitor the mass transfer and the GW spectrogram.

Mass transfer: Because of the high mass ratios considered in this work, one might expect mass transport between the two NSs during the inspiral prior to merger. In our last work [29] we estimated the amount of material flowing from one star to the other by measuring how much mass is inside the Cartesian refinement boxes. Now, we estimate the mass transfer by computing the change of baryonic mass inside a coordinate sphere around the center of the NS. The center of the NS is defined as the minimum of the lapse. We perform the integration for different coordinate radii $r_{c,\text{min}} = 8.0$ up to $r_{c,\text{max}} = 13.0$ in steps of $\Delta r_c = 0.5$. While a radius chosen too small does not cover all of the tidally deformed star, if the radius is chosen too large the mass measurement will be effected by the other star a significant time before the actual merger. We will focus on the radii $r_{c1} = r_{c2} = 10.5$.

Merger remnant: In agreement with the literature, e.g. [62], we define the merger remnant as a hypermassive neutron star (HMNS) if its rest-mass is larger than the maximum rest-mass of a stable uniformly rotating star with the same EOS; or as a supramassive neutron star (SMNS) if its rest-mass is smaller than the maximum rest-mass of a stable uniformly rotating star, but above the mass of a stable TOV-star. In case its mass is also below the maximum supported mass of a TOV-star, we call it simply a massive neutron star (MNS). Notice that these definitions *cannot* be used strictly and should be seen as a qualitative description since they refer to equilibrium configurations assuming barotropic EOS and axisymmetry.

For a HMNS the merger remnant collapses on a dynamical timescale to a BH. Typically the lifetime τ is the time from the moment of merger to the time an apparent horizon forms. The final BH is characterized by its horizon mass M_{BH} and dimensionless spin j_{BH} .

The accretion disk around the BH has a mass of

$$M_{\text{disk}} = \int_{r > r_{\text{AH}}} d^3x q^{(D)}, \quad (2)$$

with $q^{(D)} = \sqrt{\gamma}D$ where D is the fluid’s rest frame baryonic mass, γ the determinant of the 3-metric, and the domain of integration excludes the spherical region inside the apparent horizon.

Mass ejecta: As in [29] we label material as ejecta when

$$u_t < -1 \quad \text{and} \quad \bar{v}_r = v^i x_i > 0, \quad (3)$$

where $u_t = -W(\alpha - \beta_i v^i)$ is the first lower component of the fluid 4-velocity with the lapse α , the shift β^i , and the Lorentz factor W . and $x^i = (x, y, z)$. Equation (3) assumes that the fluid elements follow geodesics and requires that the orbit is unbound and has an outward pointing velocity, cf. also [63]. Other ways of estimating

the ejecta mass can be found in e.g. [64, 65]. The total ejecta mass is given by

$$M_{\text{ej}} = \int_{\mathcal{U}} d^3x q^{(D)}, \quad (4)$$

where the integral is computed on the region,

$$\mathcal{U} = \{x^i = (x, y, z) : u_t < -1 \text{ and } \bar{v}_r > 0\}, \quad (5)$$

on which material is unbound according to Eq. (3). The kinetic energy of the ejecta can be approximated as the difference between the total energy E_{ejecta} (excluding gravitational potential energy), the rest-mass, and the total internal energy U_{ejecta} [27, 29],

$$T_{\text{ej}} = E_{\text{ej}} - (M_{\text{ej}} + U_{\text{ej}}) = \int_{\mathcal{U}} d^3x q^{(D)} (e - 1 - \epsilon), \quad (6)$$

with $e = \alpha u^t h - p / (\rho \alpha u^t)$. Additionally, we compute the D -weighted integral of $v^2 = v_i v^i$ inside the orbital plane and in the x - z -plane,

$$\langle \bar{v} \rangle_{\rho} = \sqrt{\frac{\int_{\mathcal{U}_{z=0}} d^3x q^{(D)} v^2}{\int_{\mathcal{U}_{z=0}} d^3x q^{(D)}}}, \quad (7)$$

$$\langle \bar{v} \rangle_z = \sqrt{\frac{\int_{\mathcal{U}_{y=0}} d^3x q^{(D)} v^2}{\int_{\mathcal{U}_{y=0}} d^3x q^{(D)}}}, \quad (8)$$

and the D -weighted integrals

$$\langle v \rangle_{\rho} = \sqrt{\left(\frac{\int_{\mathcal{U}_{z=0}} d^3x q^{(D)} v^x}{\int_{\mathcal{U}_{z=0}} d^3x q^{(D)}} \right)^2 + \left(\frac{\int_{\mathcal{U}_{z=0}} d^3x q^{(D)} v^y}{\int_{\mathcal{U}_{z=0}} d^3x q^{(D)}} \right)^2} \quad (9)$$

and

$$\langle |v| \rangle_{\rho} = \sqrt{\frac{\int_{\mathcal{U}_{z=0}} d^3x q^{(D)} (v^x)^2}{\int_{\mathcal{U}_{z=0}} d^3x q^{(D)}} + \frac{\int_{\mathcal{U}_{z=0}} d^3x q^{(D)} (v^y)^2}{\int_{\mathcal{U}_{z=0}} d^3x q^{(D)}}} \quad (10)$$

$$\langle |v| \rangle_z = \sqrt{\frac{\int_{\mathcal{U}_{y=0}} d^3x q^{(D)} (v^z)^2}{\int_{\mathcal{U}_{y=0}} d^3x q^{(D)}}}. \quad (11)$$

Our velocity measurements can be interpreted in the following way: $\langle \bar{v} \rangle_{\rho, z}$ is the mean velocity of the ejected material inside the orbital, but not necessarily in the direction of the cylindrical radius, and perpendicular to it, $\langle |v| \rangle_{\rho, z}$ gives the average velocities, and $\langle v \rangle_{\rho}$ gives an estimate of the “kick” velocity produced by the ejecta.

Furthermore we consider the entropy “indicator”,

$$\hat{S} = \frac{p}{K_i \rho^{\Gamma_i}}, \quad (12)$$

where Γ_i and K_i are locally determined by the density ρ and the EOS. In cases where the additional thermal contribution to the pressure p_{th} is small $\hat{S} \sim 1$, while in presence of shock heating $\hat{S} \gg 1$.

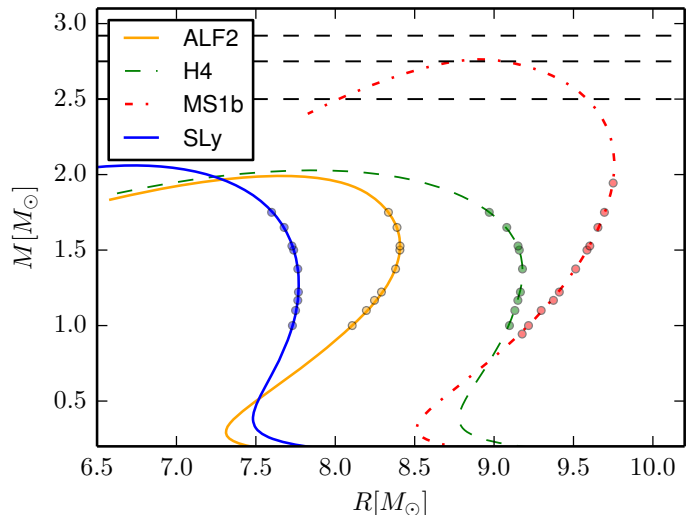


FIG. 1. The four different EOSs employed in this work. The EOSs are modeled by piecewise-polytropic fits to the tabulated EOSs. The fits are taken from [49], see also Tab. I. Markers correspond to spherical individual stars in our configurations, and dashed black lines the total masses M of our configurations for which we investigate all four EOSs. In the figure, we do not include the total mass of the setup MS1b-094194, since for those masses only the EOS MS1b was employed.

III. BNS CONFIGURATIONS

Our configurations span the mass ratios $q = 1.0, 1.25, 1.5, 1.75$ and total binary masses of $M = 2.5, 2.75, 2.9167 M_{\odot}$. For each pair (q, M) we simulate the four EOS ALF2, H4, MS1b, SLy EOS, cf. Tab. I. Additionally, we consider a $q = 2.06$ configuration with the stiff EOS MS1b, simulated at a single resolution in [20]. The mass-radius relations of each of the considered EOS are shown in Fig. 1, where we also include as markers the isolated star configurations, and as black dashed lines the total masses $M = M^A + M^B$ of the systems.

The properties of the initial configuration are listed in Tab. II. Among various quantities, we report the tidal polarizability coefficient

$$\kappa_2^T = 2 \left(\frac{q^4}{(1+q)^5} \frac{k_2^A}{C_A^5} + \frac{q}{(1+q)^5} \frac{k_2^B}{C_B^5} \right), \quad (13)$$

which describes at leading order the NSs tidal interactions, and depends on the EOS via the quadrupolar dimensionless Love number k_2 of isolated star configurations, e.g. [66]. In Eq. (13), C^A is the compactness of star A defined as the ratio of the gravitational mass in isolation M^A with the star’s proper radius. It has been shown in [67, 68] that κ_2^T is the relevant parameter encoding all the EOS information to characterize the BNS dynamics during both the merger and the postmerger phases. In addition, the GW of BNS is almost entirely determined by the mass ratio q and the κ_2^T , because the binary total mass scales trivially in absence of tides and its de-

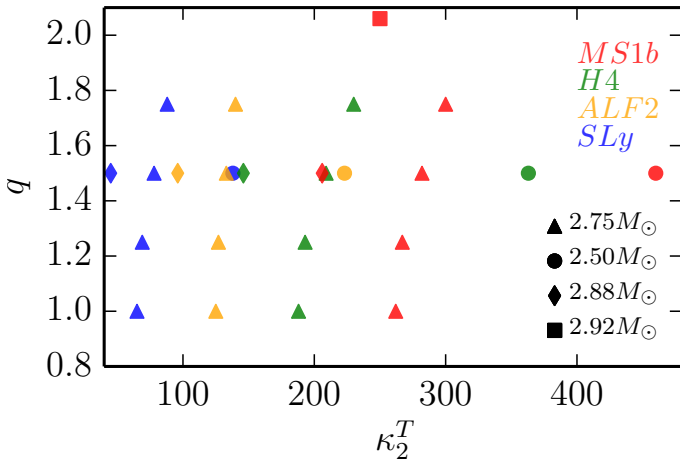


FIG. 2. BNS parameter space in terms of q and κ_2^T . Different colors represent different EOSs, while different markers stand for different total masses.

TABLE I. Properties of the equations of state (EOSs) used in this work. Our EOSs use a crust with $\kappa_{\text{crust}} = \kappa_0 = 8.94989 \times 10^{-2}$ and $\Gamma_{\text{crust}} = 1.35692$. The divisions for the individual parts are at $\rho_1 = \rho_{\text{crust}} \times 10^{-4}$, $\rho_2 = 8.11322 \times 10^{-4}$ and $\rho_3 = 1.61880 \times 10^{-3}$. The columns refer to: the name of the EOS, the maximum density in the crust, the three polytropic exponents Γ for the individual pieces, and the maximum supported gravitational mass M^{max} , maximum baryonic mass M_b^{max} , and maximum dimensionless compactness C^{max} , respectively, of an isolated nonrotating star.

EOS	ρ_{crust}	Γ_1	Γ_2	Γ_3	M^{max}	M_b^{max}	C^{max}
SLy	2.36701	3.005	2.988	2.851	2.06	2.46	0.31
ALF2	3.15280	4.070	2.411	1.890	1.99	2.32	0.26
H4	1.43709	2.909	2.246	2.144	2.03	2.33	0.26
MS1b	1.83977	3.456	3.011	1.425	2.76	3.35	0.31

pendency in the tidal waveform is hidden in the κ_2^T . Although other tidal polarizability parameters, corresponding to higher-than-quadrupole interactions, do play a role in the detailed modeling of the GW [69–71], the leading order κ_2^T encodes the main effect and it is the only tidal parameter measurable in GW searches. The coverage of the q - κ_2^T parameter space by our simulations is shown in Fig. 2.

All our configurations are simulated with at least two resolutions to control numerical artifacts and to have (at least rough) estimate of error bars for *all* the quantities. The specific grid setups can be found in Tab. II.

IV. DYNAMICS

A. Mass transfer

MS1b-094194: We reported in [20] for MS1b-094194-R1s that a rest mass up to $\approx 10^{-2}M_\odot$ was transferred

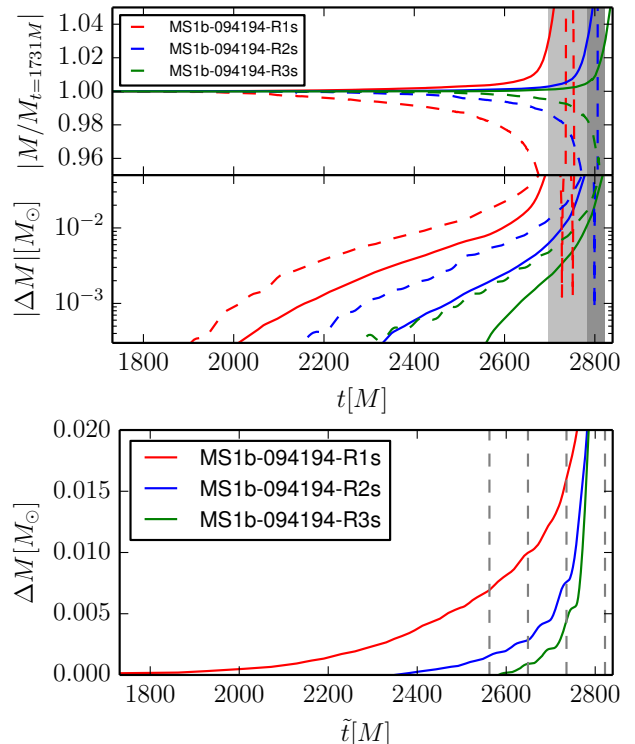


FIG. 3. Mass-transfer between the two neutron stars. Top: The panels show the time evolution of the baryonic mass and the “mass defect” $|\Delta M| = |M(t) - M(t = 5000M_\odot)|$ inside coordinate spheres of radius $10.5M_\odot$ around the two neutron stars as a function of the simulation time t . While the mass is increasing for the primary star (solid lines) the secondary star “looses” mass (dashed lines). For comparison we rescale everything to the mass at $t = 5000M_\odot$, with this approach only influences at the late stage of the inspiral are taken into account. Note that the dashed line can be seen as an upper bound for the mass transfer, since mass is also lost due to ejecta. Bottom: mass transfer as a function of the shifted time \tilde{t} , such that the moment of merger happens at the same time \tilde{t}^{mrg} for all models. The gray vertical dashed lines refer to the times shown in Fig. 4

between the stars during the last orbits before the actual merger. However, our previous investigations suffered from two facts, which we already mentioned in [20]: (i) we used a relatively low resolution (quite similar to the R1 setup); (ii) the infrastructure to compute baryonic masses inside coordinate spheres around the NSs was not implemented and the mass transfer was estimated by investigating mass changes across Cartesian refinement boxes. Here, we can investigate the mass transfer in more detail using higher resolutions. We find that the mass transfer is not robust for varying resolution, and the amount of mass decreases at higher resolutions.

We compute the baryonic mass around the NSs inside coordinate spheres of $r_{c1} = r_{c2} = 10.5M_\odot$. While for the more massive star a mass increase is directly related to the accretion of material, a mass loss of the less massive star is also produced by material ejected prior to merger.

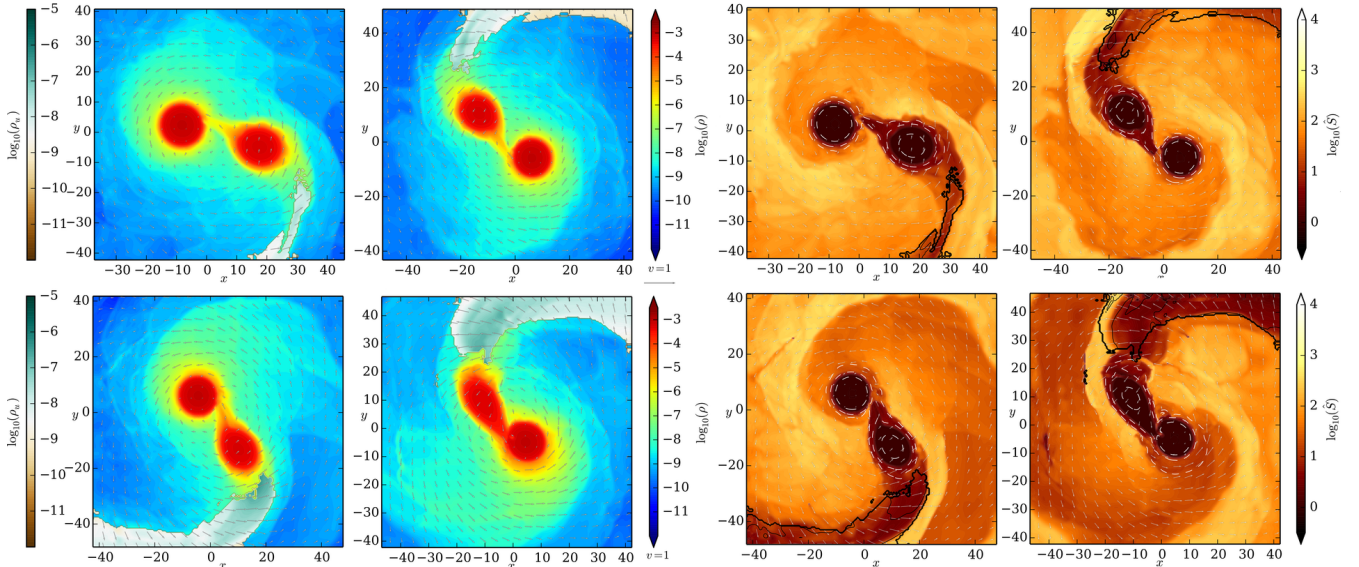


FIG. 4. Density and entropy on the orbital plane for MS1b-094194 in the final merger phase. Left plots: Density profile inside the orbital plane. The presented times are: $(2562.3, 2648.9, 2735.5, 2822.0)M$ for the upper left, upper right, lower left, lower right panel respectively. Those times correspond to the times marked in Fig. 3 as vertical dashed lines. We color the density from blue to red and the unbound density from brown to green. During the inspiral mass is ejected from the tidal tail of the less massive star due to torque. The upper right panel corresponds to the moment of merger. Right plots: Entropy indicator \hat{S} inside the orbital plane for MS1b-094194. The times are the same as in the right panels. We also include white contour lines for densities $\rho = 10^{-6}, 10^{-5}, 10^{-4}$ and black lines for the ejecta material with $\rho_u = 10^{-12}, 10^{-11}, 10^{-10}, 10^{-9}, 10^{-8}, 10^{-7}, 10^{-6}, 10^{-5}$. During the simulation we observe that the entropy between the two neutron stars is small, i.e. no shock heating produced ejecta can be observed for this setup at the chosen times.

Figure 3 summarizes our findings. The upper panel shows the baryonic mass inside $r_{c1/2}$ rescaled to the value at $t \approx 5000M_\odot \approx 1731M$. We decided not to rescale the mass with respect to the initial data to study only mass changes within a few revolutions prior to merger to allow an easier investigation. The middle panel shows the mass difference in solar masses with respect to the mass at $t \approx 1731M$. The solid lines indicate the mass gain of the more massive star, while the dashed lines show the mass loss of the secondary NS. For increasing resolution the transferred mass decreases, while for R1s we observe a mass difference of $\sim 10^{-2}$, the transferred mass decreases up to a factor of 10 for R3s.

Due to different numerical dissipation for different resolutions the moment of merger, i.e. the peak in the GW amplitude, differs. For a more simplified and straight forward comparison of the different configurations, we compensate this effect by applying a time rescaling according to $\tilde{t} = \eta t$, where the factor η is the quotient $t_{R3}^{\text{mrg}}/t_{RX}^{\text{mrg}}$ with $X = 1, 2$. t^{mrg} denotes the moment of merger, see also [72].

Thus the merger happens for all simulations at the same time \tilde{t}^{mrg} and we can easily compare the transferred mass for different resolutions. To give an impression about the density profile during the simulation, we show the rest mass density inside the orbital plane at the times $\tilde{t} = 2562.3M(7400M_\odot), 2648.9M(7650M_\odot), 2735.5M(7900M_\odot), 2822.0M(8150M_\odot)$ in Fig. 4. Those

times are also marked inside Fig. 3 (bottom panel) as vertical dashed lines. The bottom panel of Fig. 3 shows the mass gain of the more massive star over the time \tilde{t} . In total, we estimate the transferred mass to be smaller than $5 \times 10^{-3}M_\odot$. Furthermore, while the lower resolution simulation suggested that the mass transfer sets in several revolutions before the merger, mass is only transferred ~ 2 revolutions before merger for the R3 setup. In addition to the amount of transferred mass it is also interesting whether the mass transfer could heat up the more massive NS. To investigate this, we are showing the entropy indicator \hat{S} , cf. Eq.(12), together with contour density lines (white dashed) in Fig. 4. According to the entropy indicator \hat{S} no shocks are produced at the surface of the more massive star. Consequently this region of the NSs does not become significantly hotter than other parts.

Other configurations: Our discussion about the mass transfer is based on MS1b-094194, but similar results can be obtained for other configurations. Most notably, we can verify that with increasing the resolution from R1 to R2 the transferred mass is decreasing. Our simulations are also in agreement with the naive understanding that for stiff EOSs and higher mass ratios the transferred mass is increasing. Motivated by this observation, we conclude that the mass transfer estimated from the setup MS1b-094194 can be seen as an upper bound for astrophysical

realistic systems. Because of this finding together with the fact that no shocks are produced due to mass accretion to the massive neutron star, we do not expect that for astrophysical realistic systems the energy released by the mass-transfer might lead to EM counterparts which could be observed before the actual merger of the BNS system.

B. Ejecta

The mass ejection in our simulations is caused by two effects. i) Part of the unbound mass is expelled either during the (partial) tidal disruption or from the tidal tail of the companion by a centrifugal effect, see e.g. Fig. 4. These ejecta are emitted already during the last orbits in an essentially adiabatic way (small entropy value). As shown in simulations that includes microphysics e.g. [32, 73], the composition is rich in neutrons and has a small electron fraction. ii) Part of the unbound mass is expelled when the two NS cores collide. These shock-triggered ejecta are characterized by large entropy values and a higher electron fraction. The two components are clearly distinguishable by plotting the entropy indicator \hat{S} , Eq. (12). Mechanism i) is dominant for configurations with large q .

In addition to the amount of ejecta, we also compute the kinetic energy, as well as the average velocity, cf. Sec. II C. The results are summarized in Tab. III. In the following we will present two exemplary cases before discussing the general influence of the mass ratio and total mass. We often assign an uncertainty as given by the difference between different resolutions. It is however important to notice that this does not necessarily corresponds to the total uncertainty since systematic errors are significant [29]. Most notably, when the fluid expands it is possible that the density falls below the artificial atmosphere value producing mass losses in ejecta. Additionally material can also leave the grid, see Appendix A. These are the reasons why the estimated ejecta quantities are evaluated at a time, where most of the ejected material is rather close to the center of the system, at a distance of $\approx 150\text{--}250M_\odot$. While the ejected mass does not depend much on this fact, the momenta and velocities of the ejecta are typically overestimated due to fact that the gravitational potential of merger remnant is neglected in Eqs. (6)–(11). A simple Newtonian estimate shows that the ejecta velocities and the linear momenta are therefore overestimated by up to 20–30%.

MS1b-094194: Figure 4 (left panels) presents the 2D density profile of MS1b-095194 (ρ from blue to red) and the unbound density (ρ_u from brown to green). The largest amount of ejecta comes from the tidal tail of the less massive NS, i.e. mechanism i) described above. We also present snapshots of the entropy indicator \hat{S} in Fig. 4 (right panels). The density is marked as

white thin, dashed contour lines and the ejecta by black contours. From the plots it is clear that no shock heating happens inside the tidal tail. The low entropy value suggests that for such large mass ratios and stiff EOS, the ejected material will be neutron rich as found in e.g. [32].

SLy-137137: As an opposite scenario, we present the results for SLy-137137, an equal mass NSs described by a soft EOS. Figure 5 shows \hat{S} for SLy-137137-R1 inside the x - z -plane for $t = 2708M, 2714M, 2721M$ and inside the orbital plane (x - y -plane) at $t = 2721M$. The colors and contour lines are identical to the ones used in Fig. 4. The first three panels show an ejection of material, colored by black contour lines in an angle $\gtrsim 45^\circ$ to the orbital plane. The ejection is triggered from high entropic regions near the surface of the NS (white dashed lines). Also, we find that after the collision of the cores the central region of the HMNS in the orbital plane is low entropic; this suggests that no hot core forms during the merger, but that instead the hot material is confined in streams of matter expanding from the NS-NS interface and at the HMNS surface (see also [30]). Type ii) ejecta are triggered from these regions.

Effect of the mass-ratio: Figure 6 (top panel) shows the dependence of the mass of the ejected material for different mass ratios. We mainly focus on simulations with a total mass of $M = 2.75M_\odot$, but also include the MS1b-094194, which has a total mass of $M = 2.888M_\odot$ to support our argumentation. Different EOSs are represented by different colors and the uncertainty is given as an error bar based on the difference between different resolutions solely (cf. error discussion above). We find that for stiff EOSs more mass is ejected for larger mass ratios. This is in-line with previous studies [27, 29], although the mass ratios considered here are significantly larger. The trend in q is almost linear regarding MS1b (red circles), H4 EOS (green circles), ALF2 (orange circles). A rather similar dependence on the mass ratio was already found for BHNS scenarios, e.g. [74, 75], for the ejecta and the disk mass, but up to our knowledge, never presented for BNS configurations. For soft EOSs (SLy) no strong correlation between the mass-ratio and the ejected mass is visible, all the configurations produce the same amount of ejecta between $1\text{--}2 \times 10^{-2}M_\odot$.

Figure 6 (middle panel) shows the dependence of the kinetic energy as a function of the mass ratio for the $M = 2.75M_\odot$ and $M = 2.888M_\odot$ configurations. As for the amount of ejected material it is obvious that for stiff EOSs a higher mass ratio leads to ejecta with a higher kinetic energy. Again the relation between T_{ej} and q is almost linear.

Figure 6 (bottom panel) shows the estimated velocities of the ejecta inside the orbital plane and orthogonal to the orbital plane. We find that the velocity of the ejecta inside the orbital plane are $\langle |v_\rho| \rangle \sim 0.17 \sim 50000\text{km/s}$ for all configurations independent of the EOS and the

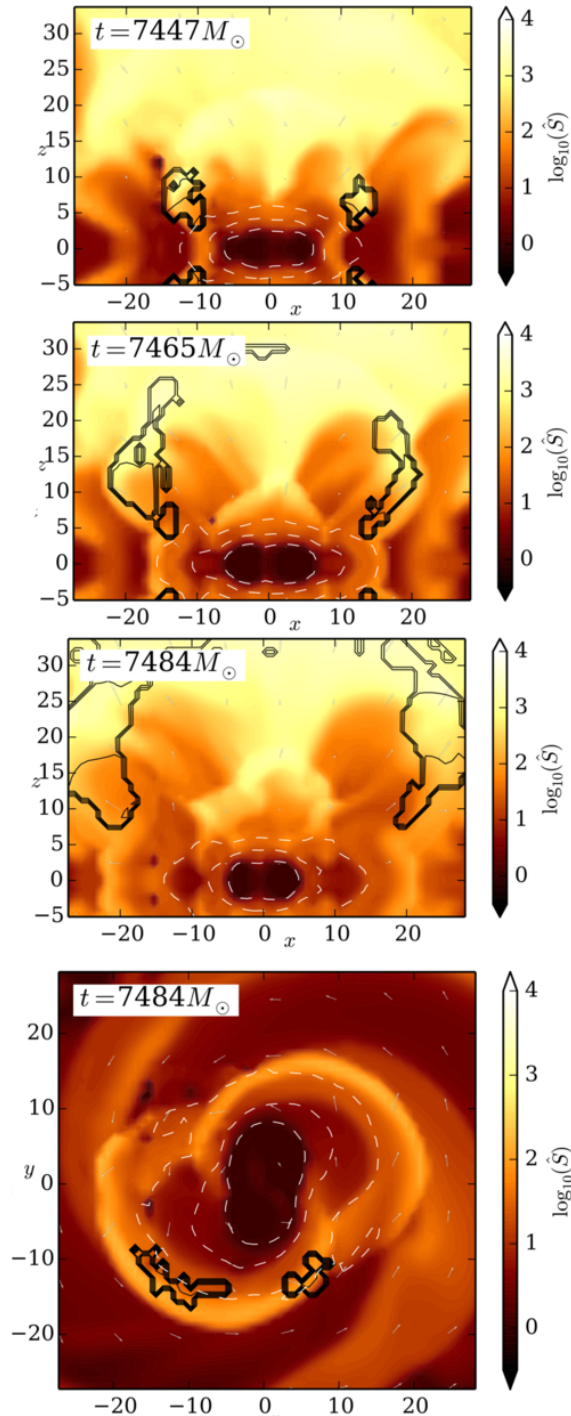


FIG. 5. Entropy indicator \hat{S} for SLy-137137 in the early postmerger phase. The panels represent snapshots at $t = 2708M$, $t = 2714$, $2721M$ from top to bottom in the x - z -plane. The last panel shows the entropy inside the orbital plane at $t = 2721M$. We also include white contour lines for densities $\rho = 10^{-6}, 10^{-5}, 10^{-4}$ and black lines for the ejecta material with $\rho_u = 10^{-12}, 10^{-11}, 10^{-10}, 10^{-9}, 10^{-8}, 10^{-7}, 10^{-6}, 10^{-5}$.

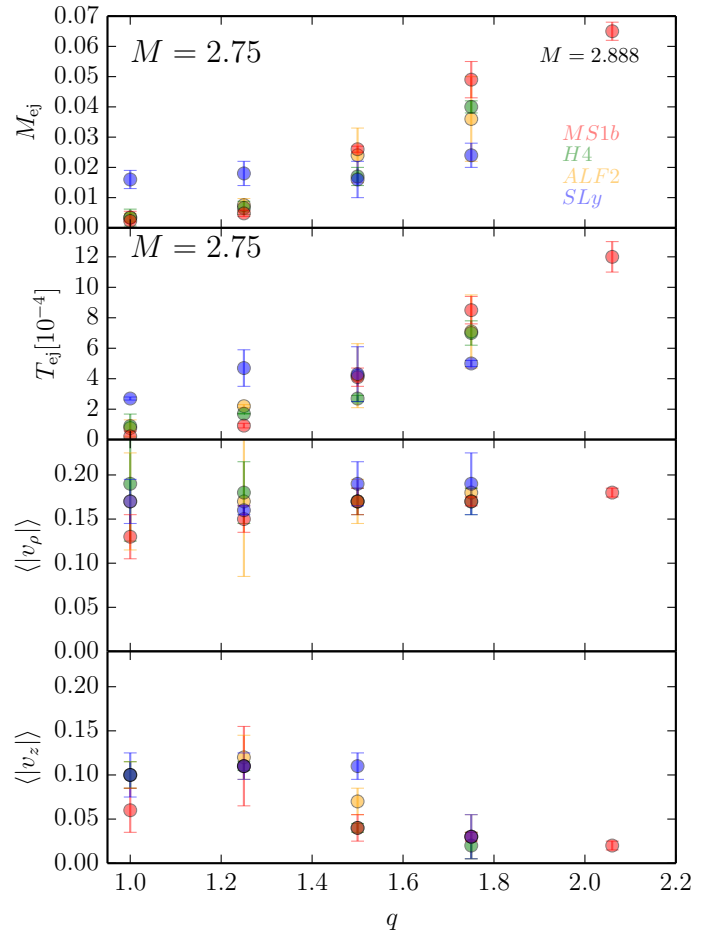


FIG. 6. Ejected properties as a function of the mass ratio for masses $M = 2.75$ and $M = 2.888$. We show the difference between two adjacent resolutions as an error bar in our plot. Top: Ejecta mass, where we see that for an increasing mass ratio stiffer EOS produce significantly more ejecta, while a similar effect can not be observed for softer EOS. Upper middle: Kinetic energy of the ejecta, where for an increasing mass ratio ejecta have significantly more kinetic energy, in particular for stiff EOSs. Lower middle: $\langle |v_\rho| \rangle$, Eq. (10), as a function of q . Bottom: $\langle |v_z| \rangle$, Eq. (11), as a function of q . While the velocity inside the orbital plane seems to be almost constant independent of the mass ratio, the velocity orthogonal to the orbital plane decreases for higher mass ratios.

mass ratio. However, we stress again that the ejecta velocities are typically overestimated with our current approach. The velocity orthogonal to the orbital plane is in general smaller than $\langle |v_\rho| \rangle$. Furthermore, we find that, independent of the EOS and above $q = 1.25$, $\langle |v_z| \rangle$ decreases for an increasing mass ratio. This suggests that for large mass ratio configurations more ejection happens inside the orbital plane than in other directions. The effect is expected since ejecta due to shock heating play a subdominant role in those cases. Furthermore this leads to a more oblate and less isotropic shape of the ejecta.

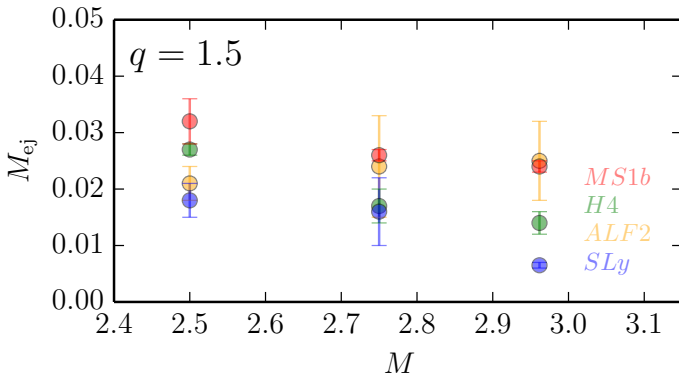


FIG. 7. Ejected mass as a function of the total mass of the binary system for a mass ratio of $q = 1.5$. We show the difference between two adjacent resolutions as an error bar. The influence of the total mass is smaller than the effect of the mass ratio, however, less ejecta are produced for higher total masses in most cases.

Effect of the total mass: Finally, we study the influence of the total mass on the amount of ejected material. For this purpose we compare all our configurations with a mass ratio of $q = 1.5$. We have evolved these configurations for total masses of $M = 2.5M_{\odot}$, $M = 2.75M_{\odot}$, and $M \approx 2.92M_{\odot}$. The data show that the influence of the total mass is smaller than the influence of the mass ratio, see Fig. 7. However, for increasing total mass, less massive ejecta are produced in agreement with previous studies, e.g. [27]. The reason for this is that larger mass systems form more compact and more massive merger remnants and the material is more bound by the larger gravitational potential.

The dependence of the kinetic energy on the total mass can be read off from Tab. III. Similarly to the ejecta mass, the kinetic energy is decreasing for higher total masses, although the uncertainties are even larger than for the mass of the ejecta. For the velocities of the ejecta no strict statement about the influence of the total mass can be made according to our simulations because of the large uncertainties.

C. Merger Remnant

Tab. IV summarizes the merger outcome (second column) and the properties of the merger remnant. In most cases (15 configurations) the merger remnant is a HMNS, which is temporarily stabilized from collapse by thermal pressure and centrifugal support. The HMNS will collapse within a dynamical timescale to a BH; this happens within the simulated time for 9 configurations. 3 configurations undergo a prompt collapse and for 7 cases the centrifugal support is sufficient to support a MNS or SMNS. In the following we discuss the lifetime of the HMNSs and the properties of the final BH and disk structure.

Lifetime of the merger remnant: The collapse time of the merger remnant is very sensitive to numerical error and grid resolution, e.g. [76]. Precise numbers are difficult to obtain, and uncertainties can be of the order of several milliseconds. From Tab. IV one observes that a larger total mass of the system leads to an earlier collapse, as expected by the fact that a larger rest-mass star is closer to the collapse threshold.

The influence of the EOS is less clear than the effect of the total mass, however, as outlined in [29] one can expect that systems with a softer EOSs collapse earlier than systems with a stiff EOS. The EOSs SLy, ALF2, H4 EOS support approximately the same maximum mass regarding single spherical stars, cf. Fig. 1 and Tab. I. But, the stiffer the EOS, the longer is the lifetime of the HMNS. Binaries with stiffer EOS are in general less bound at merger than soft EOSs binaries. This fact has been quantified in [67], that computed universal relations of the binary’s binding energy and angular momentum at formation of the merger remnant as functions of the parameter κ_2^T , Eq. (13). A consequence of those relations is that stiffer EOS lead to binaries with larger centrifugal support. In addition to the centrifugal support, the pressure support in the central regions is larger for stiffer EOS, and the merger remnant is even further stabilized.

Focusing on the effect of the mass-ratio on the lifetime of the remnant, we observe for several cases that larger q give slightly larger lifetimes. Regarding, e.g., setups employing the H4 EOS we find that the equal mass setup collapses to a BH, but the HMNSs formed during the merger of most of the unequal mass systems survive until the end of the simulation. However, for a more conclusive statement we suggest that higher resolution are needed since for several setups the differences in the lifetime of the merger remnant caused by different mass ratios lie within the error bar obtained from different resolutions. For larger q the merger remnant is typically more non-axisymmetric than for equal-mass configurations, and thus has a larger angular momentum support. Also, looking again at Eq. (13), for fixed EOS (k_2) and fixed masses, larger q correspond to larger κ_2^T . Using the relations of [67], this implies indeed that remnants from binaries with larger q have larger angular momentum at formation.

Final black hole and disk: For 12 configurations a black hole has formed during our simulations, and we expect that if we evolved our configurations for longer the remaining 6 HMNS would have formed a BH as well. In cases where a BH forms we also report the BH mass M_{BH} , the dimensionless spin j_{BH} of the BH and the mass of the accretion disk M_{disk} .

The mass of the BH depends trivially on the mass of the binary systems, i.e. more massive systems produce more massive BHs. Regarding M_{BH}/M , we find that for systems with $M = 2.75M_{\odot}$ at a time $t = t^{mrg} + 250M_{\odot}$ M_{BH} is $\sim 88\%$ - up to 91% of the total mass. For systems with a total mass of $M \approx 2.92$ at $t = t^{mrg} + 250M_{\odot}$ the

TABLE III. Ejecta properties. The columns refer to: the name of the configuration, the mass of the ejecta, the kinetic energy of the ejecta, the D -weighted integral v_ρ , Eq. (9), the average velocity of the ejecta inside the orbital plane $\langle |v| \rangle_\rho$ and perpendicular to it $\langle |v| \rangle_z$, cf. Eqs. (10) and (11), and the average of v^2 of fluid elements inside the orbital plane $\langle \bar{v} \rangle^\rho$ and perpendicular to it $\langle \bar{v} \rangle^z$, Eqs. (7) and (8). We present results for R2 resolved runs and give R1 results inside brackets for an error estimate. (With the exception of MS1b-094194, where we give results for R3 and R2.)

Name	$M_{\text{ej}} [10^{-2} M_\odot]$	$T_{\text{ej}} [10^{-4}]$	v_ρ	$\langle v \rangle_\rho$	$\langle v \rangle_z$	$\langle \bar{v} \rangle^\rho$	$\langle \bar{v} \rangle^z$
ALF2-137137	0.34 (0.20)	0.76 (0.22)	0.066 (0.058)	0.17 (0.12)	0.10 (0.11)	0.17 (0.12)	0.22 (0.15)
H4-137137	0.34 (0.06)	0.89 (0.10)	0.039 (0.080)	0.19 (0.13)	0.10 (0.14)	0.19 (0.13)	0.23 (0.22)
MS1b-137137	0.23 (0.55)	0.22 (0.56)	0.030 (0.032)	0.13 (0.11)	0.06 (0.08)	0.13 (0.11)	0.14 (0.14)
SLy-137137	1.6 (1.3)	2.7 (2.8)	0.060 (0.042)	0.17 (0.19)	0.10 (0.12)	0.17 (0.19)	0.17 (0.20)
ALF2-122153	0.75 (0.97)	2.2 (2.1)	0.077 (0.089)	0.17 (0.09)	0.12 (0.10)	0.17 (0.09)	0.23 (0.17)
H4-122153	0.66 (0.88)	1.7 (1.7)	0.032 (0.002)	0.18 (0.15)	0.11 (0.11)	0.18 (0.16)	0.22 (0.28)
MS1b-122153	0.48 (0.58)	0.92 (0.77)	0.038 (0.104)	0.15 (0.14)	0.11 (0.07)	0.16 (0.14)	0.20 (0.21)
SLy-122153	1.8 (1.4)	4.7 (3.5)	0.014 (0.076)	0.16 (0.16)	0.11 (0.10)	0.16 (0.16)	0.22 (0.21)
ALF2-100150	2.1 (1.8)	2.7 (1.9)	0.095 (0.092)	0.15 (0.14)	0.07 (0.06)	0.15 (0.14)	0.15 (0.15)
H4-100150	2.7 (2.6)	4.5 (3.0)	0.130 (0.084)	0.17 (0.14)	0.03 (0.04)	0.17 (0.15)	0.16 (0.15)
MS1b-100150	3.2 (2.8)	4.4 (2.8)	0.124 (0.078)	0.16 (0.14)	0.03 (0.04)	0.16 (0.14)	0.17 (0.13)
SLy-100150	1.8 (1.5)	5.1 (1.8)	0.095 (0.023)	0.19 (0.14)	0.12 (0.06)	0.19 (0.14)	0.23 (0.14)
ALF2-110165	2.4 (1.5)	4.2 (2.1)	0.101 (0.088)	0.17 (0.15)	0.07 (0.08)	0.17 (0.15)	0.18 (0.16)
H4-110165	1.7 (2.0)	2.7 (2.9)	0.123 (0.105)	0.17 (0.16)	0.04 (0.04)	0.17 (0.16)	0.18 (0.17)
MS1b-110165	2.6 (2.5)	4.1 (3.5)	0.126 (0.101)	0.17 (0.16)	0.04 (0.05)	0.17 (0.16)	0.16 (0.17)
SLy-110165	1.6 (1.0)	4.3 (2.5)	0.064 (0.054)	0.19 (0.17)	0.11 (0.12)	0.19 (0.18)	0.21 (0.24)
ALF2-117175	2.5 (1.8)	6.0 (4.9)	0.100 (0.088)	0.19 (0.16)	0.06 (0.09)	0.18 (0.18)	0.20 (0.20)
H4-117175	1.4 (1.6)	2.6 (2.6)	0.125 (0.105)	0.18 (0.17)	0.05 (0.06)	0.19 (0.17)	0.19 (0.17)
MS1b-117175	2.4 (2.5)	4.3 (3.9)	0.108 (0.099)	0.18 (0.16)	0.05 (0.08)	0.18 (0.16)	0.17 (0.19)
SLy-117175	0.65 (0.60)	3.1 (1.6)	0.118 (0.063)	0.25 (0.14)	0.11 (0.07)	0.38 (0.15)	0.24 (0.20)
ALF2-100175	3.6 (5.0)	7.1 (9.5)	0.118 (0.113)	0.18 (0.18)	0.03 (0.05)	0.19 (0.19)	0.21 (0.17)
H4-100175	4.0 (4.2)	7.0 (6.2)	0.131 (0.106)	0.17 (0.16)	0.02 (0.03)	0.18 (0.17)	0.29 (0.18)
MS1b-100175	4.9 (5.5)	8.5 (9.4)	0.134 (0.115)	0.17 (0.17)	0.03 (0.03)	0.18 (0.17)	0.19 (0.18)
SLy-100175	2.4 (2.8)	5.0 (4.8)	0.096 (0.044)	0.19 (0.16)	0.03 (0.05)	0.21 (0.16)	0.21 (0.22)
MS1b-094194	6.5 (6.8)	12 (13)	0.130 (0.126)	0.18 (0.18)	0.02 (0.02)	0.18 (0.18)	0.17 (0.21)

BH mass is 89%–94% of the total mass. Interestingly for the irreducible mass $M_{\text{irr}} = \sqrt{A_{\text{BH}}/(16\pi)}$ (with A_{BH} being the horizon area) we find that M_{irr}/M is almost independent of the EOS, mass, and mass ratio and takes a value around ~ 0.85 for all setups. As the final BH mass, also the final dimensionless spin of the BH j_{BH} is larger for more massive systems, see Tab. IV and lies around ~ 0.7 for our systems with a mass of $2.92M_\odot$. On the other hand, the imprint of the mass-ratio on the mass and spin of the BH is less clear. We find that the black hole mass is almost independent of the mass-ratio and that the dimensionless spin is slightly decreasing for an increasing mass ratio, cf. in particular the systems employing the ALF2 EOS. The decrease in the dimensionless spin is caused by the fact that outer region and the formed disk has larger angular momentum. Among the different EOS considered and for fixed mass ratio and total mass, the ALF2 EOS produces in most cases a faster rotating black hole than the other configurations.

We find in our simulations that, for configurations un-

dergoing prompt collapse, the system has no sufficient time to redistribute angular momentum to outer regions. Thus, the formed disk is less massive. In other configurations that form a HMNS, larger q give more massive disks [26, 77]. In Fig. 8 we present the disk mass as a function of time after BH formation for the ALF2 configurations up to $q = 1.50$ with $M = 2.75$. The disk mass increases up 30% comparing $q = 1$ and $q = 1.75$. We find that in general disks produced by larger mass ratios have smaller maximum densities, but a larger radii. For SLy no monotonic trend is present in our simulations.

V. GRAVITATIONAL WAVES

GWs are calculated extracting the curvature invariant Ψ_4 on coordinate spheres and computing projections on the spin-weighted spherical harmonics for spin -2 , $-2Y_{lm}$, see e.g. [42]. The metric multipoles $rh_{\ell m}$ are reconstructed from the curvature multipoles using the fre-

TABLE IV. Properties of the merger remnant. The columns represent: (i) the classification of the merger remnant; (ii) the lifetime in case a HMNS has formed and collapsed during our simulation (given in multiples of $100M_\odot$) or a description as ‘p.c.’ for a prompt collapse of the remnant; (iii) the final mass of the BH M_{BH} ; (iv) the dimensionless spin of the final BH j_{BH} ; (v) the mass of the disk surrounding the BH M_{disk} measured $250M_\odot$ after BH formation. We mark runs where the apparent horizon finder did not work reliably with a * and runs where no BH has formed for one resolution but for the other with **.

Name	remnant	τ [$100M_\odot$]	$M_{BH}[M_\odot]$	j_{BH}	$M_{disk}[M_\odot]$
ALF2-137137	HMNS→BH	26 (24)	2.49 (2.50)	0.65 (0.65)	0.20 (0.17)
H4-137137	HMNS→BH	42 (39)	2.44 (*)	0.59 (*)	0.23 (0.11)
MS1b-137137	MNS	-	-	-	-
SLy-137137	HMNS→BH	77 (36)	2.42 (2.43)	0.60 (0.61)	0.23 (0.21)
ALF2-122153	HMNS→BH	23 (**)	2.48 (**)	0.64 (**)	0.23 (**)
H4-122153	HMNS	-	-	-	-
MS1b-122153	MNS	-	-	-	-
SLy-122153	HMNS→BH	33 (29)	2.44 (2.45)	0.59 (0.60)	0.20 (0.20)
ALF2-100150	HMNS	-	-	-	-
H4-100150	HMNS	-	-	-	-
MS1b-100150	MNS	-	-	-	-
SLy-100150	HMNS	-	-	-	-
ALF2-110165	HMNS→BH	21 (42)	2.48 (2.40)	0.61 (0.57)	0.24 (0.30)
H4-110165	HMNS	-	-	-	-
MS1b-110165	MNS	-	-	-	-
SLy-110165	HMNS→BH	58 (**)	2.45 (**)	0.61 (**)	0.26 (**)
ALF2-117175	BH	p.c.	2.70 (2.67)	0.71 (0.70)	0.20 (0.21)
H4-117175	HMNS→BH	14 (17)	2.65 (2.62)	0.68 (0.65)	0.26 (0.24)
MS1b-117175	SMNS	-	-	-	-
SLy-117175	BH	p.c.	2.75 (2.73)	0.73 (0.72)	0.14 (0.15)
ALF2-100175	HMNS→BH	25 (26)	2.48 (2.42)	0.61 (0.57)	0.26 (0.29)
H4-100175	HMNS	-	-	-	-
MS1b-100175	MNS	-	-	-	-
SLy-100175	BH	p.c.	* (*)	* (*)	0.18 (0.21)
MS1b-094194	SMNS	-	-	-	-

quency domain integration of [78]. The initial circular GW frequency is used as a cutting frequency. The GW strain is then given by

$$h(t, \theta, \phi) = \sum_{l=2}^{l_{\max}} \sum_{m=-l}^l r h_{lm}(t)^{-2} Y_{lm}(\theta, \phi), \quad (14)$$

where we include individual modes up to $l_{\max} = 4$. All waveforms are plotted against the retarded time,

$$u = t - r_* = t - r_{\text{extr}} - 2M \ln(r_{\text{extr}}/2M - 1), \quad (15)$$

where the extraction radius is set to $r_{\text{extr}} \sim 1000 M_\odot$. As explained in [53] for such an extraction radius the error compared to extrapolated waveforms is $\lesssim 0.5\%$ for the amplitude and below 0.1 rad for the phase of the GW. The GW energy radiated during the simulations is calculated as

$$\mathcal{E}_{\text{rad}} = \sum_{l,m}^{l_{\max}} E_{l,m} = \frac{1}{16\pi} \sum_{l,m}^{l_{\max}} \int_0^t dt' \left| r \dot{h}_{lm}(t') \right|^2, \quad (16)$$

with $l_{\max} = 8$. We also define the m -mode contributions as

$$E_m := \sum_{l=m}^{l_{\max}} E_{lm}. \quad (17)$$

The *total* GW energy emitted during the binary history is given by

$$E_{\text{rad}}^{\text{tot}} = M - M_{\text{ADM}}(t=0) + \mathcal{E}_{\text{rad}}. \quad (18)$$

In addition to the waveforms, we compute spectra and spectrograms by applying the Fourier transform \mathcal{F} (in fact, the discrete FFT) and compute the power spectral density (PSD) of the GWs as in [76],

$$\tilde{h}_{lm}(f) = |\mathcal{F}[h_{lm}(t)]|, \quad (19)$$

$$\tilde{h}(f; \theta, \phi) = |\mathcal{F}[h(t; \theta, \phi)]|. \quad (20)$$

The spectrogram allows to identify to which part of the wave [and so of the dynamics] the spectrum peaks correspond to. They are computed with chunks of width

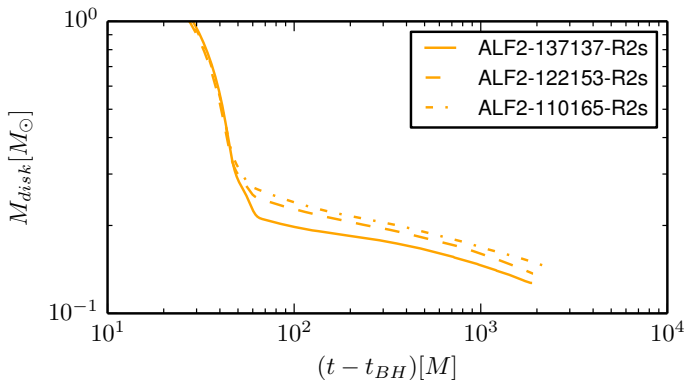


FIG. 8. Rest mass of the disk surrounding the final BH for the ALF2 configurations with a mass of $M = 2.75$ and mass ratios $q = 1.0; 1.25, 1.5$. Clearly visible is that for an increasing mass-ratio the disk is more massive. However, ALF2-100175 and ALF-110165 give almost the same disk masses. We have not included ALF2-100175 in this figure since the simulation after the collapse to the BH is much shorter than for the other configurations.

$\Delta t = 400M_{\odot}$. Note also that \tilde{h} depends on the inclination θ and azimuthal angle ϕ , i.e. the location of the detector with respect to our source. For most of our analysis we pick $\theta = \pi/4$ and $\phi = 0$, i.e., the line of sight to the detector is 45° above the orbital plane. But, we will also consider one BNS configuration for which we investigate the influence of θ on \tilde{h} .

Figure 9 shows the real part of the dominant (2,2) multipole for our configurations, where the solid colored lines represent the highest resolved runs (R2) and the dashed black lines the lower resolution (R1). The signal is composed by the well-known chirp corresponding the inspiral-to-merger transition, which formally ends at the wave amplitude’s peak, followed by the post-merger emission which corresponds to the HMNS/MNS-phase. In some simulations the signal also contains the collapse to the BH and the quasi-normal ringing.

Table V reports the number of orbits from the start of the simulation to the end of the chirp, $u := u_{\text{mrg}}$, defined as the time of the h_{22} amplitude peak. We also report there the GW frequency at u_{mrg} as f_{mrg} . We find that the dimensionless frequency at merger $M\omega_{\text{mrg}}$ depends on the EOS and the mass ratio. While stiffer EOSs merge with a lower frequency, softer EOSs merge at higher frequencies. Furthermore, higher mass ratios lead to smaller merger frequencies. This behavior is understood in terms of the leading order tidal coupling constant κ_2^T , and can be encoded with high precision in the quasi-universal relations proposed in [67].

In the following, we discuss spectra, spectrograms, and GW energy focusing on the post-merger phase. Similar analysis have been reported in e.g. [76, 79–81]. GW from unequal-masses BNS, in particular, have been computed recently in e.g. [27, 32, 68, 82].

A. Spectrograms

We present the spectrograms for our configurations in Fig. 10. The color bar goes from red to blue and is given in arbitrary units, since we are only interested in the frequencies and the relative strength. Additional information are given in Table V.

During the inspiral-merger one observes the typical chirp signal, with frequency and amplitude increasing monotonically over time. The end of the chirp, $u = u_{\text{mrg}}$, is marked by an amplitude peak followed by a sharp amplitude’s cut-off. The (2,2)-mode is by far the most dominant mode emitting more than 99% of the total energy. Thus, higher modes can not be seen when \tilde{h} is considered, but can be studied looking at \tilde{h}_{lm} (see below).

The postmerger spectra are mainly characterized by a dominant emission frequency f_2 , related to the (2,2)-mode. A prominent secondary peak in the (2,2) channel is also visible at frequency $f_s < f_2$ for several configurations (see also Fig. 11 below). Interpretation of the latter have been proposed in e.g. [79, 81–83] and references therein. Our spectrograms indicate the peak originates during the very early postmerger phase, right after the GW amplitude peak that marks the end of the chirping signal (inspiral-merger), see e.g. the panel of MS1b-137137 for $u \sim 3000M$. During this short period the waveforms are characterized, in addition to the oscillation at frequency f_2 , by an amplitude modulation corresponding to the fluid’s mass axisymmetric mode.

Notably, for larger mass ratios the spectra becomes more complicated as shown in Fig. 11. At fixed EOS and M , the peak of the spectra for larger q has less power and more peaks appear at frequencies $f_{\text{mrg}} < f < f_2$. The secondary peak, in particular, at f_s has maximum power for $q = 1$ and progressively disappears for larger values $q > 1$. Correspondingly, we checked that, for large q , the fluid’s mass axisymmetric oscillations diminish (see also the wave’s amplitude in Fig. 9).

By considering the multipolar waveforms \tilde{h}_{lm} , and not only the (2,2) mode, we observe other modes excited during the postmerger. These mode frequencies are named f_1, f_3, \dots, f_m and roughly correspond to the azimuthal $m = 1, 2, 3, \dots$ modes of oscillations of the fluid¹. These frequencies are more robustly extracted in the “late” postmerger phase, i.e. few milliseconds after the waveform amplitude peak. For a clear interpretation we extract the f_1 frequency from the (2,1) and the f_3 -frequency from the (3,3) mode, but they are present in all the GW multipoles unless killed for symmetry reason in the projection integrals.

¹ To avoid confusion, we explicitly mention the difference between our f_1 and f_3 frequency and the one defined in [82]. However, we decided to stick to the notation used in [29, 84], since this notation is better suited once more than just the dominant (2,2)-mode is considered.

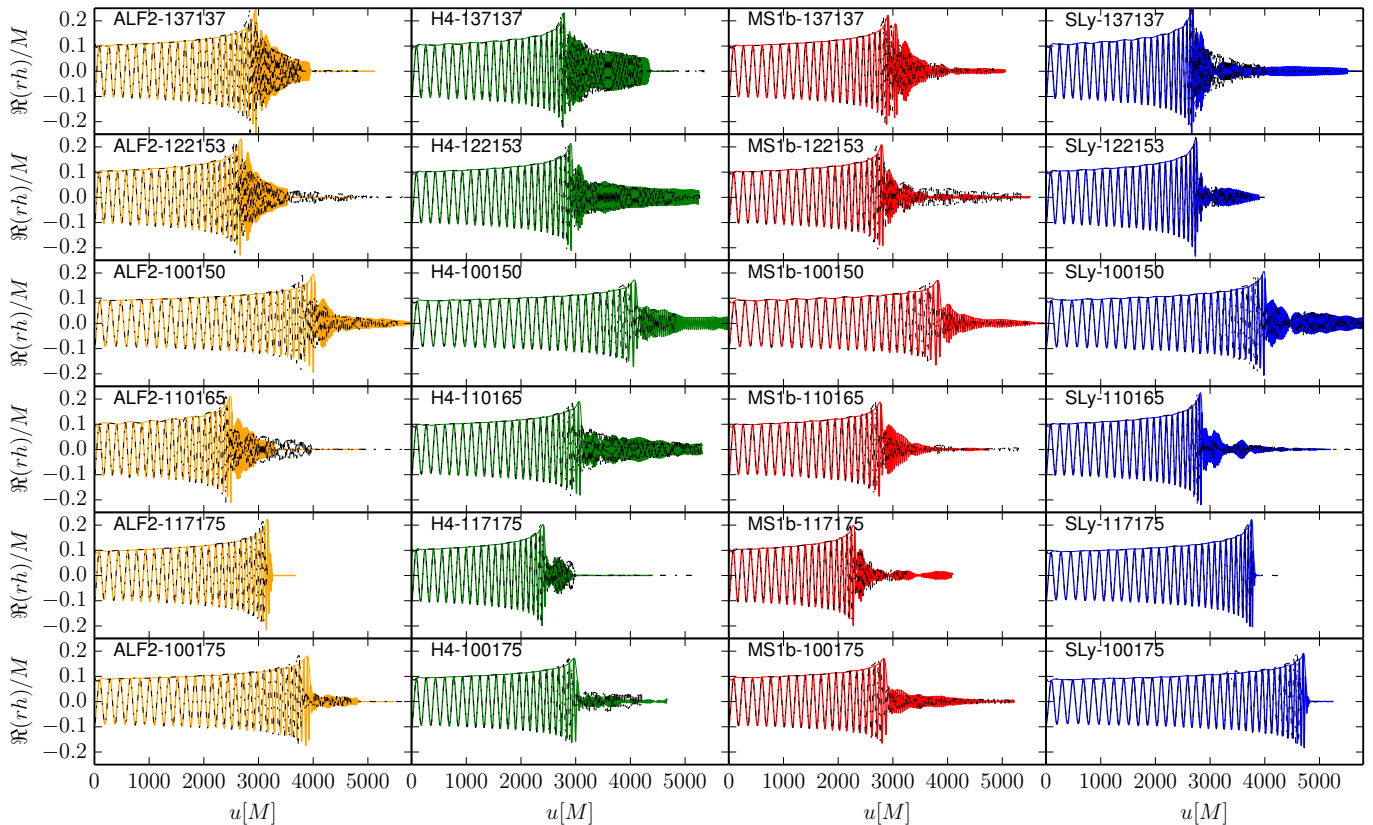


FIG. 9. Real part and amplitude of the (2,2)-multipole $h_{lm}(u)$ of the GWs for different configurations and the highest resolution. Different colors correspond to different EOS: ALF2 is orange, H4 green, MS1b red, and SLy blue. The lower resolution runs are shown as a black dotted line to understand the influence of the resolution in our configurations.

As a further illustration of the multipoles effect, we present \tilde{h}_{lm} for H4-137137-R2 in Fig. 12. We have rescaled the individual contributions for better visibility (we multiplied \tilde{h}_{21} and \tilde{h}_{33} by $10^{2.5}$ and \tilde{h}_{44} by $10^{3.5}$). In this case it is clear that the (2,2) mode is dominated by the f_2 frequency, the (2,1)-mode by f_2 and f_1 , the (3,3)-mode by f_2 and f_3 , and for the (4,4)-mode we find peaks at the f_2, f_3, f_4 frequency. As expected the frequency of the (4,4)-mode during the inspiral-merger is approximately twice the frequency of the (2,2)-mode. This harmonicity of the frequencies is also present in the post-merger phase.

Let us specify the spectrogram features for each of the different postmerger scenarios.

MNS/SMNS waveforms: For the configurations employing the MS1b EOS, the merger remnant is a stable MNS or a SMNS, see lines for the total mass of the systems in Fig. 1. The spectrogram is dominated by the frequency f_2 , but one can clearly see contributions from other multipoles in the $m = 1, 3$ and even the $m = 4$ channels. The emission of energy and angular momentum decreases over time, as also visible in Fig. 9 by a decreasing amplitude. Characteristic timescales for the GW emission have been identified in [30].

HMNS waveforms: In cases of a HMNS and, in particular for configurations undergoing gravitational col-

lapse within dynamical times, the postmerger signal is shorter and peaks at specific frequencies f_1, f_2, f_3 are more difficult to extract than for MNS/SMNS. Considering the f_2 -frequency one clearly observes a “postmerger-chirp”, i.e. that the frequency increases over time up to the formation of the BH, cf. Fig. 11 for $q = 1$ H4². But contrary to the inspiral the postmerger-chirp is characterized by a decreasing amplitude. The feature is physically expected from the increase of rotational velocity and compactness of the star over time [68]. We observe it in all our configurations. We stress that this indicates that spectra are actually *continuous*, and they can be modeled with discrete frequencies only for cases in which the remnant lifetime is sufficiently long so that most of the GW energy is radiated at frequencies close to f_2 . This timescale is $\gtrsim 20$ ms [30].

Prompt Collapse waveforms: In cases of a prompt collapse to a BH, the spectra/spectrograms have cut-off after the chirp with no other signal. Since no additional refinement levels are added once the BH forms, the resolution around the puncture is lower than in our BH simulations [42]. Thus although the quasi-normal ringing is

² Note that the wiggles for $f > 2500$ Hz are just due to the Fourier transform of the finite-length signal.

TABLE V. GW quantities. The columns refer to: the name of the configurations, the number of orbits until merger from the beginning of the simulation estimated as $N_{\text{orb}} = \Phi^{\text{mrg}}/4\pi$ with Φ^{mrg} being the accumulated phase, the dimensionless merger frequency $M\omega_{\text{mrg}}$, the merger frequency in kHz f_{mrg} , the dominant postmerger frequencies for extracted from the (2,1),(2,2),(3,3)-mode, and a possible secondary peak in the (2,2)-mode. Also these frequencies are stated in kHz. In cases where no secondary peak is found, we mark this simulations with $-$. We abbreviate the prompt collapse of some configurations with p.c.. Results in brackets refer to R1 resolved runs expect for MS1b-094194, where we show results for R2 in brackets.

Name	N_{orb}	$M\omega_{\text{mrg}}$	f_{mrg}	f_1	f_2	f_3	f_s
ALF2-137137	11.7 (11.2)	0.144 (0.142)	1.72 (1.70)	1.55 (1.46)	2.80 (2.77)	4.30 (4.06)	1.70 (1.70)
H4-137137	10.9 (10.7)	0.133 (0.127)	1.59 (1.52)	1.27 (1.38)	2.50 (2.58)	3.74 (3.84)	1.61 (1.74)
MS1b-137137	10.9 (10.7)	0.121 (0.118)	1.45 (1.41)	1.06 (1.06)	2.14 (2.06)	3.10 (3.07)	1.58 (1.57)
SLy-137137	11.4 (11.2)	0.167 (0.163)	2.00 (1.95)	1.83 (1.76)	3.66 (3.47)	5.39 (5.16)	2.80 (2.56)
ALF2-122153	10.9 (10.4)	0.133 (0.131)	1.59 (1.57)	1.42 (1.44)	2.72 (2.68)	4.11 (4.13)	2.41 (2.43)
H4-122153	11.1 (10.9)	0.114 (0.115)	1.36 (1.38)	1.28 (1.24)	2.42 (2.38)	3.78 (3.70)	1.75 (-)
MS1b-122153	10.6 (10.2)	0.110 (1.08)	1.32 (1.29)	1.07 (1.08)	2.02 (2.16)	3.12 (3.24)	1.82 (1.80)
SLy-122153	11.3 (11.3)	0.143 (0.144)	1.71 (1.72)	1.65 (1.66)	3.30 (3.36)	5.09 (5.04)	2.91 (3.00)
ALF2-100150	13.8 (12.9)	0.106 (0.103)	1.37 (1.33)	1.19 (1.20)	2.44 (2.38)	3.69 (3.60)	-
H4-100150	13.4 (12.8)	0.086 (0.084)	1.11 (1.09)	1.15 (1.05)	2.20 (2.10)	3.25 (3.05)	-
MS1b-100150	13.4 (12.8)	0.084 (0.084)	1.11 (1.11)	1.00 (0.95)	1.95 (1.95)	2.90 (2.95)	-
SLy-100150	14.3 (13.6)	0.114 (0.111)	1.51 (1.47)	1.46 (1.43)	2.96 (2.87)	4.40 (4.23)	2.59 (2.54)
ALF2-110165	10.2 (9.8)	0.119 (0.118)	1.40 (1.39)	1.45 (1.32)	2.74 (2.74)	4.17 (4.06)	1.89 (1.95)
H4-110165	11.6 (10.9)	0.101 (0.098)	1.19 (1.15)	1.28 (1.24)	2.57 (2.43)	3.83 (3.54)	-
MS1b-110165	10.4 (10.0)	0.098 (0.096)	1.15 (1.13)	0.99 (1.06)	1.94 (1.98)	3.00 (3.02)	-
SLy-110165	11.6 (11.3)	0.133 (0.130)	1.56 (1.53)	1.76 (1.62)	3.51 (3.51)	5.25 (5.04)	2.31 (-)
ALF2-117175	12.4 (12.0)	0.131 (0.127)	1.45 (1.41)	p.c.	p.c.	p.c.	p.c.
H4-117175	9.9 (9.6)	0.110 (0.109)	1.22 (1.21)	1.38 (1.36)	2.82 (2.80)	4.21 (4.05)	1.95 (1.90)
MS1b-117175	9.3 (9.0)	0.109 (0.110)	1.21 (1.22)	1.11 (1.04)	2.09 (1.99)	3.20 (3.10)	-
SLy-117175	14.6 (14.2)	0.148 (0.137)	1.64 (1.52)	p.c.	p.c.	p.c.	p.c.
ALF2-100175	14.0 (13.4)	0.106 (0.109)	1.27 (1.31)	p.c.	p.c.	p.c.	p.c.
H4-100175	11.0 (10.6)	0.089 (0.090)	1.07 (1.07)	1.25 (1.21)	2.44 (2.50)	3.77 (3.68)	-
MS1b-100175	10.4 (10.0)	0.088 (0.087)	1.05 (1.04)	0.96 (0.93)	1.98 (2.05)	3.03 (2.99)	-
SLy-100175	16.6 (15.9)	0.122 (0.105)	1.35 (1.25)	p.c.	p.c.	p.c.	p.c.
MS1b-094194	10.7 (10.5)	0.087 (0.088)	0.96 (0.97)	0.92 (1.01)	2.14 (2.00)	3.20 (3.23)	-

visible, we can only resolve between five to eight local maxima of $r\Psi_{4,22}$ after the merger. This is not sufficient to extract accurately the quasi-normal modes of the newly formed BH.

B. Source sky location

We discuss the influence of the source's sky location on the measured GW spectrum for the model H4-110165. We pick as fiducial angles $(\theta = 0, \phi = 0)$, $(\theta = \pi/4, \phi = 0)$, $(\theta = \pi/2, \phi = 0)$ and present the results in Fig. 13.

The inspiral-merger signal is strongest for $\theta = 0$, which can be explained by the fact that the (2,2)-mode contribution to h is largest for this angle since ${}^{-2}Y_{22}(\theta)$ has its maximum for $\theta = 0$. The post-merger signal is dominated by the f_2 -mode, and no f_1 frequency could be detected because ${}^{-2}Y_{21}(0) = {}^{-2}Y_{2-1}(0) = 0$. Increasing the inclination θ , the contribution from the f_2 -frequency decreases, and the detectability of the f_1 -frequency in-

creases. Note however that is unlikely the $m = 1$ modes will be detected in GW observations [84].

C. GW Energy

Finally, let us discuss the influence of the mass ratio on the emitted GW energy. The emitted energy is calculated according to Eq. (16) and we compute the contributions for all modes individually. To the end of the simulation $\sim 1-5 \times 10^{-2}M_{\odot}$ is radiated. The largest amount of energy is emitted by the (2,2)-mode, which emits 2-3 orders of magnitude more energy than other modes. The total radiated energy $E_{\text{rad}}^{\text{tot}}$ is shown in Fig. 14 at the moment of merger, i.e. u_{mrg} , (left panel), and $\sim 4000M_{\odot}$, i.e. 20ms after the merger (right panel). The thin dashed lines represent the emitted energy for a non-spinning BBH systems. To estimate the emitted energy at merger, we use the effective-one-body model of [85]. The final total energy is instead computed by the fitting formula of [86].

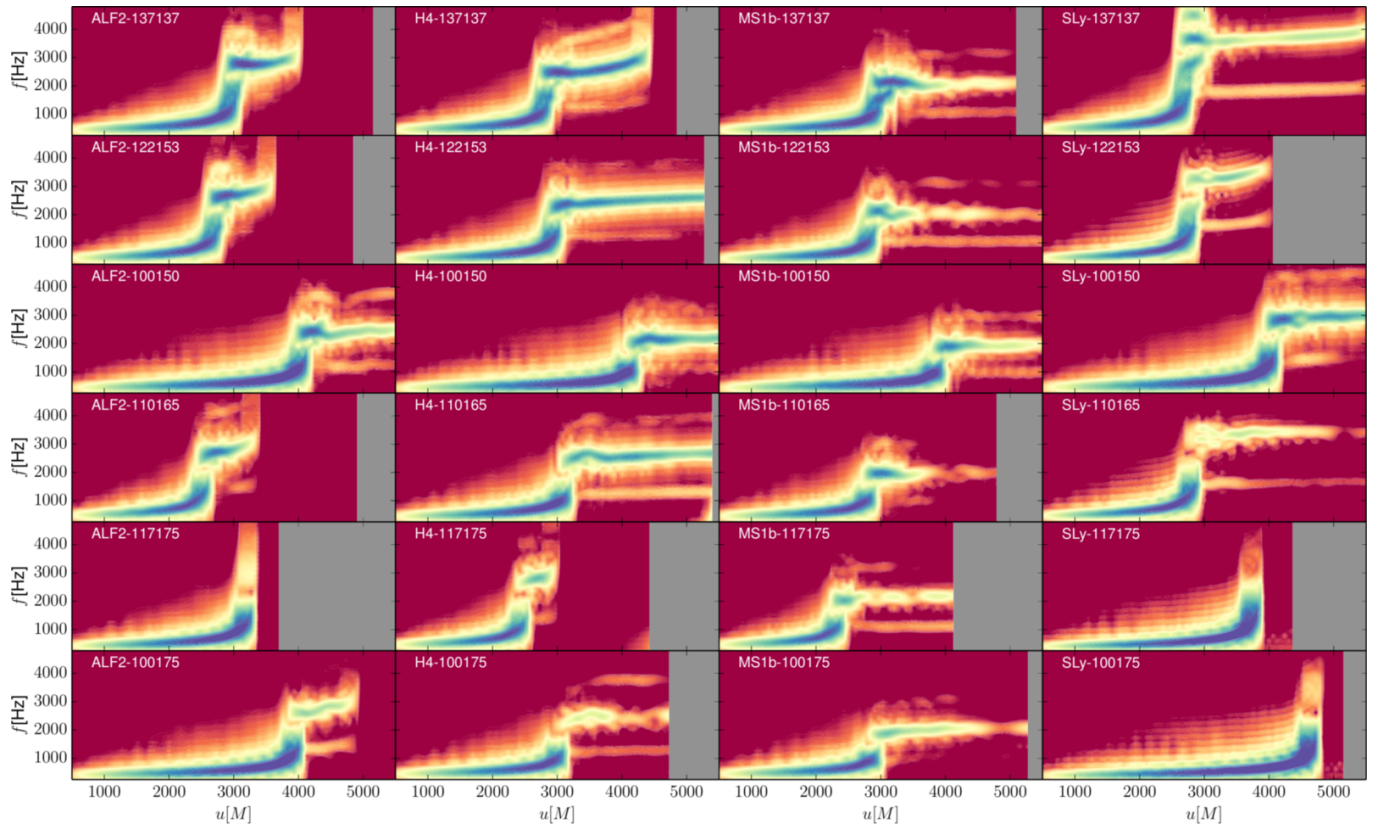


FIG. 10. Spectra $\tilde{h}(\theta = \pi/4, \phi = 0)$ for all configurations. Clearly visible is the chirp signal of the inspiral-merger phase followed by the post-merger signal (if no prompt collapse). In most of the cases, the spectrogram highlights that several frequencies, other than the f_2 , are excited in the postmerger. Note also that configurations like ALF2-137137, H4-137137, and SLy-122153, in which a HMNS forms and collapse within dynamical times, clearly shows that the postmerger spectrum is not discrete, but rather continuous, and similar to the inspiral-merger chirp.

As for BBHs, the BNS emitted energy decreases for an increasing mass ratio. Since NSs merge at larger separations and are less relativistic than corresponding BBH systems, the emitted energy at merger is smaller than the corresponding emitted energy for BBHs [30]. In the postmerger phase the influence of the mass ratio becomes even more prominent than during merger. More energy is released for equal mass systems than for unequal mass setups. We also find an imprint of the EOS, where in general NSs employing a soft EOS emit more energy than for a stiff EOS. Both observations can be explained in terms of the quasi-universal relations: systems with larger κ_2^T produce a more bound merger remnant and release more energy [67].

We present in Fig. 15 the rescaled energies E_{lm}/E_{22} for simulations with mass $M = 2.75M_\odot$ and the EOS MS1b. For equal mass configurations the second dominant mode during the inspiral-merger is the (4,4) mode followed by the (3,2)-mode, see the upper left panel of Fig. 15. All other modes do not produce a significant contribution to the total emitted energy during this phase and contribute only $\sim 0.1\%$ to the total energy up to the merger. For unequal mass configurations the important subdominant modes are (3,3), (4,4), (2,1), (3,2) in

descending order³. This is in qualitative accord to the post-Newtonian theory: the amplitudes of (3,3) and (2,1) modes are nonzero for unequal mass configurations and they are proportional to the mass ratio at leading order, e.g. [87]. In our simulations we find that for a mass ratio of $q = 1.75$ around 1% of the emitted energy comes from the (3,3) mode.

In the post-merger phase several different modes are excited. The (2,2)-mode is still dominant. At the end of our simulations the (3,3) mode is the second strongest followed by (2,1), (4,4), (3,2), (2,0), where the exact ordering depends on the mass ratio and EOS. We find that also for $q = 1$ the (2,1) and (3,3) mode are non-zero, cf. [84, 88]. Computing the luminosity $dE_{lm}(t)/dt$ (not shown in the plot) we find that while dE_{22}/dt decreases over time due to the very efficient emission in this channel [30], other modes actually increase up to the collapse time, in particular dE_{33}/dt and dE_{21}/dt , e.g. [31, 84].

³ With the exception of ALF2-100175, SLy-117175, Sly-100175, for which the (2,1) is particularly large because of center of mass drift due to the initial residual linear momentum, see Tab. VII.

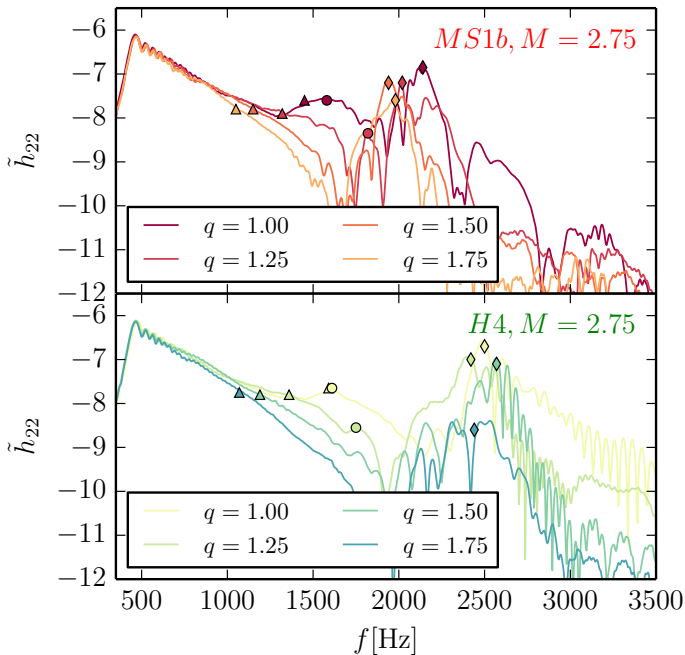


FIG. 11. Effect of mass-ratio on the GW spectra. Top: \tilde{h}_{22} for MS1b setups for mass ratios $q = 1.00; 1.25; 1.50; 1.75$. Bottom: \tilde{h}_{22} for H4 setups for mass ratios $q = 1.00; 1.25; 1.50; 1.75$. We mark the f_2 -frequencies as diamonds, the f_{mrg} as triangles and the secondary peak frequencies f_s as circles.

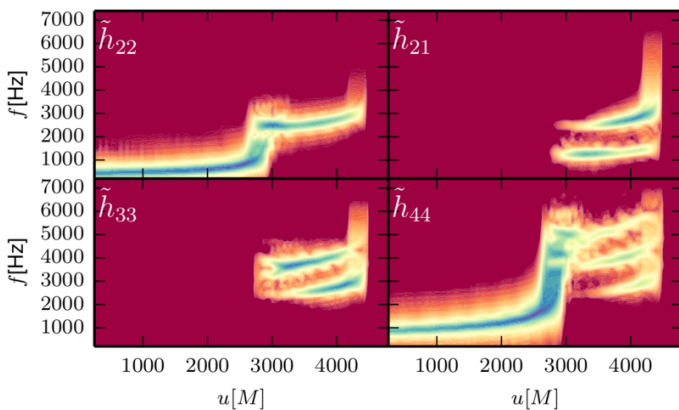


FIG. 12. Spectra of individual GW modes for H4-137137-R2 setup. We present \tilde{h}_{lm} for $(lm) = (22), (21), (33), (44)$. The amplitudes are rescaled for better visibility, i.e. \tilde{h}_{21} and \tilde{h}_{33} are rescaled by a factor of $10^{2.5}$ and \tilde{h}_{44} by $10^{3.5}$.

In Fig. 16 we present the energy released for E_m with $m = 1, 3, 4$ divided by E_2 . We see that at the merger (left panels) for an increasing mass ratio more energy is emitted for $m = 1, 3$ with respect to the total energy. For $m = 4$ the energy mode is approximately constant and contributed $\sim 0.2\%$ to the total emitted energy. The clear imprint of the mass-ratio for $m = 1, 3$ is lost after the merger (right panels). However, a small trend towards more energy release for unequal mass ratios for

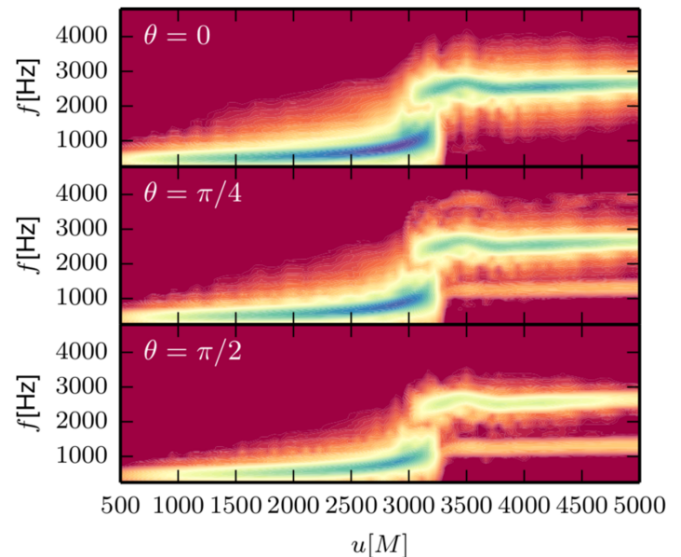


FIG. 13. Angular dependence of the GW spectra for H4-110165-R2. We present \tilde{h} for: $(\theta = 0, \phi = 0)$ (top panel), $(\theta = \pi/4, \phi = 0)$ (middle panel), and $(\theta = \pi/2, \phi = 0)$ (bottom panel).

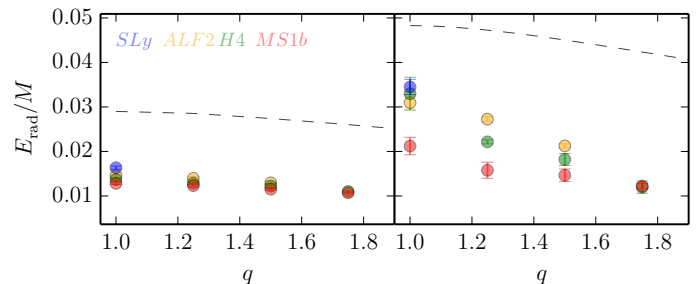


FIG. 14. Total GW energy emitted for different EOSs and mass ratios. For the total energy we also take into account contributions before the beginning of the simulation ($M - M_{\text{ADM}}(t = 0)$). Shown as dashed lines are estimates for the released energy during BBH mergers (see text for details). The left panel shows the energies at the moment of merger, i.e. peak of the GW amplitude, right panels represent data 20 ms after merger. We have removed those setups for which the initial linear momentum, Tab. VII, was large and an artificial drift of the center of mass was present.

larger mass ratios is still present for $m = 3$. In addition to the imprint of the mass ratio we find that during the postmerger phase the amount of energy emitted in the subdominant modes is much higher compared to the inspiral independent of the mass ratio. In general up to $\sim 3\%$ of the total released energy can be emitted in the subdominant modes.

VI. ELECTROMAGNETIC COUNTERPARTS

Since we do not simulate the evolution of the electron fraction and of the internal composition of the fluid, we

TABLE VI. Electromagnetic Counterparts. The columns refer to: the name of the configuration, the time in which the peak in the near infrared occurs t_{peak} , the corresponding peak luminosity L_{peak} , the temperature at this time T_{peak} , the time of peak in the radio band $t_{\text{peak}}^{\text{rad}}$, and the corresponding radio fluence. As in other tables, we present results for R2 and R3 resolved simulations and results for the second highest resolution for all configurations are given in brackets.

Name	t_{peak} [days]	L_{peak} [10^{40} erg/s]	T_{peak} [10^3 K]	$t_{\text{peak}}^{\text{rad}}$ [years]	$F_{\text{peak}}^{\nu\text{rad}}$ [mJy]
ALF2-137137	2.0 (1.8)	2.6 (1.9)	2.5 (2.7)	6.4 (6.1)	0.041 (0.007)
H4-137137	1.9 (0.9)	2.8 (1.4)	2.5 (3.3)	5.9 (3.5)	0.058 (0.005)
MS1b-137137	2.0 (3.1)	1.9 (2.5)	2.7 (2.4)	7.3 (10.6)	0.006 (0.013)
SLy-137137	4.5 (3.7)	4.5 (4.6)	1.9 (2.0)	10.0 (7.9)	0.143 (0.203)
ALF2-122153	2.9 (4.2)	3.7 (2.9)	2.2 (2.2)	8.0 (17.6)	0.139 (0.046)
H4-122153	2.7 (3.4)	3.5 (3.5)	2.2 (2.1)	7.3 (9.6)	0.105 (0.074)
MS1b-122153	2.5 (3.0)	2.9 (2.8)	2.3 (2.3)	7.2 (9.1)	0.046 (0.026)
SLy-122153	4.7 (4.2)	4.7 (4.3)	1.9 (2.0)	12.3 (11.3)	0.237 (0.173)
ALF2-100150	5.4 (5.4)	4.5 (4.0)	1.9 (1.9)	12.6 (13.6)	0.100 (0.056)
H4-100150	6.1 (6.5)	5.1 (4.6)	1.8 (1.8)	14.0 (15.7)	0.187 (0.090)
MS1b-100150	6.9 (6.9)	5.1 (4.5)	1.8 (1.8)	15.9 (17.2)	0.152 (0.072)
SLy-100150	4.5 (4.9)	5.2 (3.8)	1.9 (2.0)	9.9 (13.3)	0.359 (0.055)
ALF2-110165	5.6 (4.6)	5.0 (4.1)	1.8 (2.0)	12.8 (11.4)	0.190 (0.083)
H4-110165	4.8 (5.4)	4.3 (4.5)	1.9 (1.9)	11.8 (12.9)	0.111 (0.109)
MS1b-110165	6.1 (6.0)	5.0 (4.8)	1.8 (1.8)	14.1 (14.1)	0.161 (0.131)
SLy-110165	4.3 (3.3)	4.9 (4.0)	1.9 (2.1)	9.8 (8.3)	0.288 (0.159)
ALF2-117175	5.5 (4.9)	5.3 (4.6)	1.8 (1.9)	12.8 (13.0)	0.317 (0.233)
H4-117175	4.2 (4.7)	4.2 (4.3)	2.0 (1.9)	10.3 (11.5)	0.129 (0.108)
MS1b-117175	5.6 (5.8)	5.0 (5.0)	1.8 (1.8)	12.8 (13.0)	0.195 (0.170)
SLy-117175	2.4 (3.0)	4.1 (2.8)	2.2 (2.3)	6.0 (11.5)	0.340 (0.055)
ALF2-100175	6.9 (8.0)	5.9 (6.6)	1.7 (1.6)	14.7 (16.0)	0.340 (0.460)
H4-100175	7.4 (7.7)	5.9 (5.7)	1.7 (1.7)	16.1 (16.8)	0.293 (0.234)
MS1b-100175	8.2 (8.7)	6.3 (6.5)	1.6 (1.6)	17.1 (18.0)	0.361 (0.386)
SLy-100175	5.5 (6.3)	5.2 (5.0)	1.8 (1.8)	12.5 (15.6)	0.254 (0.177)
MS1b-094194	9.4 (9.5)	7.0 (7.2)	1.5 (1.5)	18.8 (18.5)	0.489 (0.581)

rely on simplified models for estimating the EM luminosity, fluxes and light curves. We use in particular the analytical model of [89] which assumes that the diffusion time is less than the dynamical times for computing the peak luminosity and temperature. Light-curves are computed with the model described in [75], originally introduced for the merger of BHNS systems. Radio flares peak fluxes are instead computed following [10].

Simulations including microphysics have been presented e.g. in [32, 33, 65, 90–92]. Although more detailed in term of simulated physics, none of these work have explored the effect of large q as we do here.

A. Macronovae

Following [89], we can estimate the time t_{peak} at which the peak in the near-infrared occurs, the bolometric luminosity at this time L_{peak} , and the corresponding tem-

perature T_{peak} :

$$t_{\text{peak}} = 4.9 \text{ d} \times \left(\frac{M_{ej}}{10^{-2} M_{\odot}} \right)^{\frac{1}{2}} \left(\frac{\kappa}{10 \text{ cm}^2 \text{ g}^{-1}} \right)^{\frac{1}{2}} \left(\frac{v_{ej}}{0.1} \right)^{-\frac{1}{2}}, \quad (21)$$

$$L_{\text{peak}} = 2.5 \cdot 10^{40} \text{ erg s}^{-1} \times \left(\frac{M_{ej}}{10^{-2} M_{\odot}} \right)^{1-\frac{\alpha}{2}} \left(\frac{\kappa}{10 \text{ cm}^2 \text{ g}^{-1}} \right)^{-\frac{\alpha}{2}} \left(\frac{v_{ej}}{0.1} \right)^{\frac{\alpha}{2}}, \quad (22)$$

$$T_{\text{peak}} = 2200 \text{ K} \times \left(\frac{M_{ej}}{10^{-2} M_{\odot}} \right)^{-\frac{\alpha}{8}} \left(\frac{\kappa}{10 \text{ cm}^2 \text{ g}^{-1}} \right)^{-\frac{\alpha+2}{8}} \left(\frac{v_{ej}}{0.1} \right)^{\frac{\alpha-2}{8}}. \quad (23)$$

Ref. [89] assumes that the energy release due to the radioactive decay is proportional to $\sim t^{-\alpha}$ with $\alpha = 1.3$. Furthermore, we set the average opacity to $\kappa = 10 \text{ cm}^2 \text{ g}^{-1}$ as in [89].

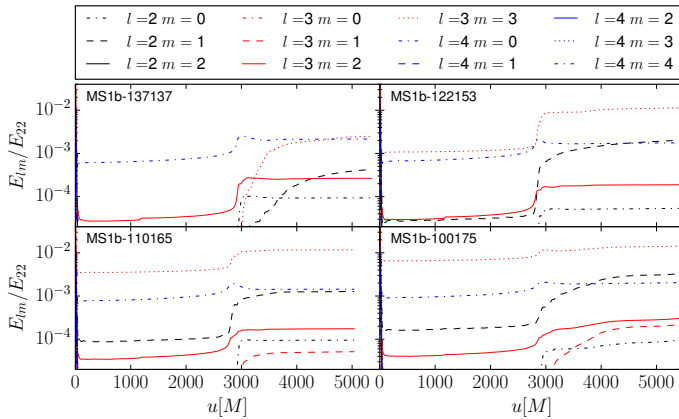


FIG. 15. GW energy emitted by different modes (up to $l = m = 4$) and rescaled by the amount of energy emitted by the (2,2)-mode. Black lines correspond to $l = 2$ contributions, red lines the $l = 3$ contributions, and $l = 4$ is represented by blue lines. Different dashing corresponds to different m . We present the configurations MS1b-137137 (upper left panel), MS1b-122153 (upper right panel), MS1b-110165 (lower left panel), MS1b-100175 (lower right panel).

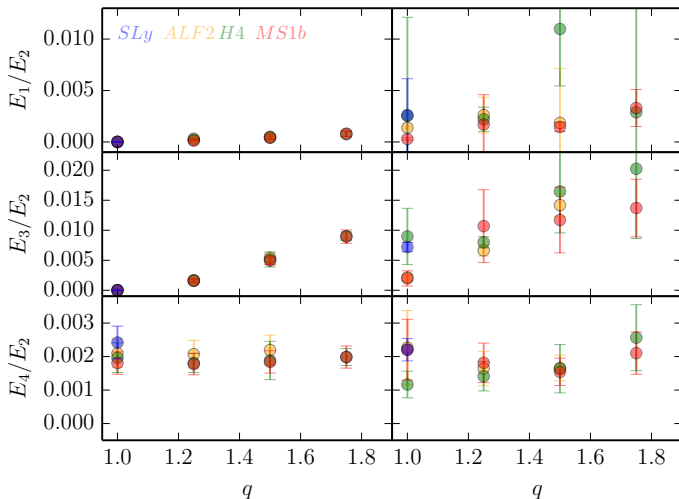


FIG. 16. GW energy emitted by different modes $E_m = \sum_{l=m}^8 E_{lm}$. We show E_m for $m = 1; 3; 4$ rescaled by E_2 . Left panels show the energies at the moment of merger, i.e. peak of the GW amplitude, right panels represent data 20 ms after merger. We have removed those setups for which the initial linear momentum, Tab. VII, was large and an artificial drift of the center of mass was present.

We summarize the time of the peak, the corresponding luminosity and temperature for our configurations in Tab. VI. Results are also shown in Fig. 17. We find that for an increasing mass ratio the peak time increases from ~ 2 days up to ~ 10 days. This effect is larger for stiffer EOSs. Also the peak luminosity increases with an increasing mass ratio. Except for the SLy setup the peak luminosity scales almost linear to the mass ratio. Finally (lower panel of Fig. 17) we see that the peak temperature

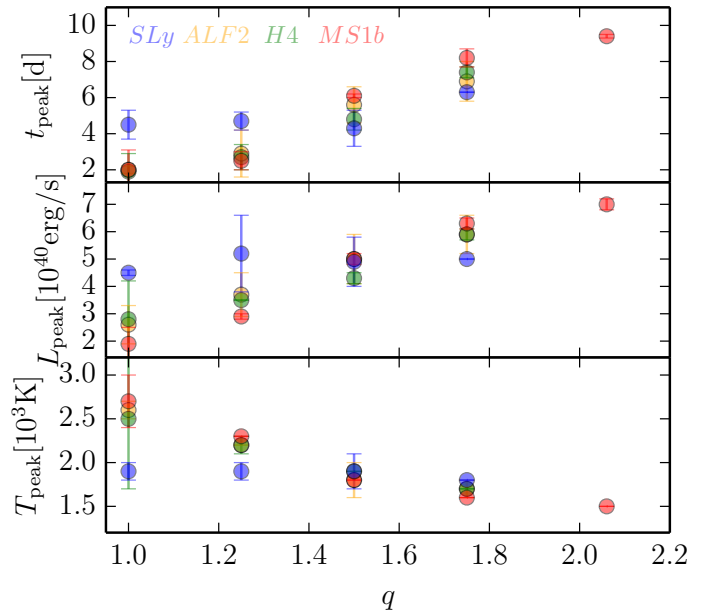


FIG. 17. Peak time t_{peak} (top panel), peak luminosity L_{peak} (middle panel), and peak temperature T_{peak} (bottom panel) of macronovae produced by the BNS mergers considered in this article as a function of the mass ratio. As before we consider configurations with $M = 2.75M_{\odot}$ and $M = 2.888M_{\odot}$.

decreases from $\sim 2500\text{K}$ to $\sim 1500\text{K}$ when the mass ratio increases, except for SLy for which the temperature for all mass ratios is around $\sim 1700\text{K}$.

Light curves are computed following [75]. The model assumes homologous expansion of the ejecta, a gray opacity, diffusion approximation for the radiation transfer and that the photons diffuse only from the latitudinal edge. It was originally developed for the EM radiation produced during the merger of a BHNS system. The main difference between the ejecta of BNS and BHNS mergers is that during BHNS mergers it is unlikely that shocks form. However, we have shown in Fig. 4 that the entropy of the ejected material for MS1b-094194 is relatively small. Similar statements hold for other configurations employing stiff EOSs. For this reason we expect that the model of [75] is appropriate for the MS1b as well as other stiff configurations and systems without shocks.

We use the publicly available program of [93]. Input parameters are taken from Tab. III. The latitude opening angles are estimated by evaluation of Eq. (19) and Eq. (20) of [29]. Furthermore, we use as longitudinal opening angle $\pi(\text{rad})$, $\kappa = 10\text{cm}^2\text{g}^{-1}$ for the opacity, $\dot{\epsilon} = 1.58 \times 10^{10}\text{erg/g/s}$ for the heating rate coefficient, $\alpha = 1.2$ for the heating rate power and $\epsilon_{th} = 0.5$ for the thermalization efficiency as in [75, 93].

Figure 18 presents our results. We find that the considered configurations will have a luminosity between $10^{39} - 10^{42}\text{erg/s}$ (upper panel). Since the luminosity strongly correlates to the mass of the ejecta, we observe that for an increasing mass ratio the luminosity increases for more than one order of magnitude for our configu-

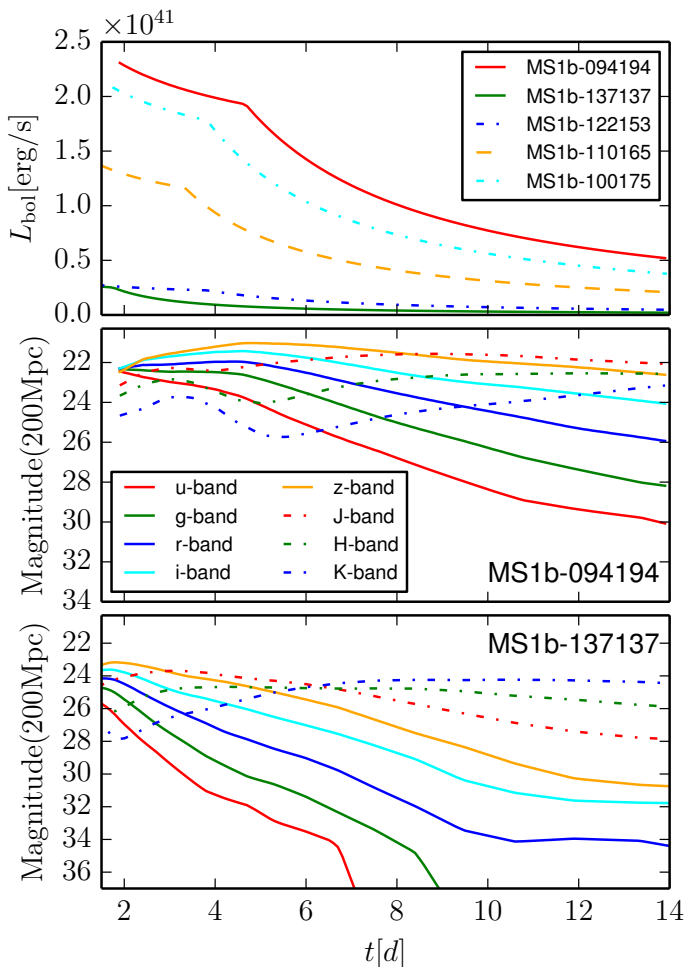


FIG. 18. Top panel: Predicted lightcurve (absolute bolometric luminosity) for the predicted macronova produced by the merger of the configurations employing the MS1b EOS. The lightcurve is produced with the publicly available code of [75]. Middle and bottom panel: absolute magnitudes for the ugrizJHK-band assuming that the macronova is produced 200Mpc away for MS1b-094194 (middle panel) and MS1b-137137 (bottom panel).

rations. Because of the increasing luminosity also the observed magnitude of the macronova at a hypothetical distance of 200Mpc is larger for MS1b-094194 (middle and bottom panel). But also for MS1b-137137 counterparts⁴ are observable for the first days after merger with 8-m class telescopes assuming that magnitudes between 26 and 27 are detectable. Contrary, for high mass ratio configurations like MS1b-094194 macronovae can be observed for several days up to weeks after the merger. Thus, the mass ratio has a clear observational imprint on the EM counterparts.

⁴ Notice that the model of [75] was tested for ejecta masses above $0.01M_{\odot}$ and that higher uncertainties and errors might be present for low mass ejecta.

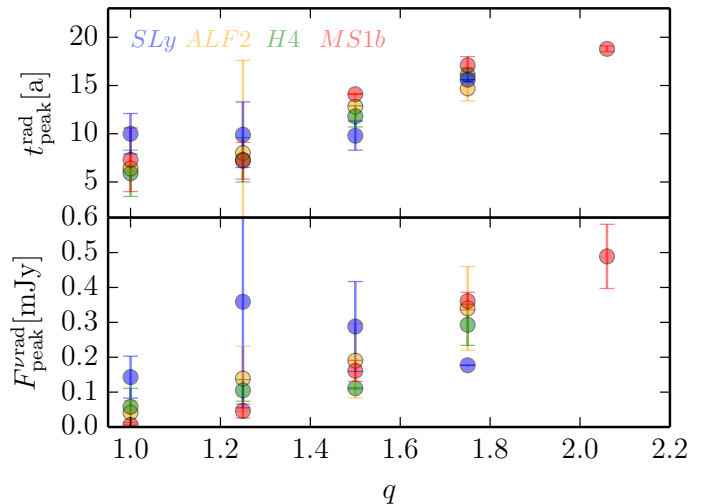


FIG. 19. Peak time in the radio band $t_{\text{peak}}^{\text{rad}}$ (top panel) and corresponding radio fluence $F_{\text{peak}}^{\nu\text{rad}}$ (bottom panel), as a function of the mass ratio. We consider BNS configurations with $M = 2.75M_{\odot}$ and $M = 2.888M_{\odot}$.

B. Radio Flares

In order to estimate the radio emission, we use the model of [10] in which the strongest signal is expected at a time

$$t_{\text{peak}}^{\text{rad}} = 1392 \text{ d} \times \left(\frac{T_{\text{ej}}}{10^{49} \text{ erg}} \right)^{\frac{1}{3}} \left(\frac{n_0}{\text{cm}^{-3}} \right)^{-\frac{1}{3}} \left(\frac{v_{\text{ej}}}{0.1} \right)^{-\frac{5}{3}} \quad (24)$$

with a radio fluence of

$$F_{\text{peak}}^{\nu\text{rad}} = 0.3 \text{ mJy} \times \left(\frac{T_{\text{ej}}}{10^{49} \text{ erg}} \right) \left(\frac{n_0}{\text{cm}^{-3}} \right)^{\frac{p+1}{4}} \left(\frac{\epsilon_B}{0.1} \right)^{\frac{p+1}{4}} \times \left(\frac{\epsilon_e}{0.1} \right)^{p-1} \left(\frac{v_{\text{ej}}}{1} \right)^{\frac{5p-7}{2}} \left(\frac{D}{10^{27} \text{ cm}} \right)^{-2} \times \left(\frac{\nu_{\text{obs}}}{1.4 \text{ GHz}} \right)^{-\frac{p-1}{2}} \quad (25)$$

for an observation frequency ν_{obs} , which is expected to be higher than the self-absorption and synchrotron peak frequency at a distance D . The parameters ϵ_B and ϵ_e determine how efficiently the energy of the blast wave is transferred to the magnetic field and to electrons. We set both parameters to $\epsilon_B = \epsilon_e = 0.1$ in our analysis as in [10]. The variable n_0 denotes the surrounding particle density and is set to 0.1 cm^{-3} . Following [10] we additionally set $p = 2.3$ and $\nu_{\text{obs}} = 1.4 \text{ GHz}$.

We report our results for $t_{\text{peak}}^{\text{rad}}$ and $F_{\text{peak}}^{\nu\text{rad}}$ in Tab. VI and in Fig. 19. As for t_{peak} , $t_{\text{peak}}^{\text{rad}}$ increases with an increasing mass ratio. The peak time $t_{\text{peak}}^{\text{rad}}$ is in the range of a few years up to two decades for very high mass ratios. The corresponding radio fluence is characterized by large uncertainties, however, for stiff EOS an almost linear growth for an increasing mass ratio is observed.

VII. SUMMARY

In this article we studied the effect of the mass-ratio by a large set of new numerical relativity simulations spanning, for the first time, up to values $q \sim 2$. Our findings are summarized in what follows.

Mass transfer: A resolution study of simulations with $q = 2$ showed that mass transfer during the last orbits is very dependent on the grid resolution. In particular, by increasing resolution the amount of transferred mass decreases. We conclude that no significant mass transfer happens during the merger of BNS, even in cases with large mass-ratio.

Mass ejection: Mass ejection in large q systems is primary due to a centrifugal effect and originates from the companion's tidal tail (or partial disruption) during the late inspiral and merger. Ejecta components due to shock-driven ejecta are only dominant for configurations with a soft EOS and rather independent of the mass ratio. We showed, for the first time in the context of BNS, that the dependence of the ejecta mass and kinetic energy is essentially linear on the mass-ratio q for stiff EOSs, see Fig. 6. Also the velocity of the ejecta depend significantly on the mass ratio. In particular, the component perpendicular to the orbital plane decreases for increasing q , since torque becomes the dominant ejecta mechanism. For large q the ejecta are almost entirely about the orbital plane. Overall, these ejecta properties for large q resemble those of black hole - neutron star binaries and lead to characteristic features of electromagnetic counterparts (see below). Finally, the total mass of the configuration plays a minor role and is less important than the EOS or the mass-ratio.

Merger remnant: The lifetime of the merger remnant depends strongly on the EOS, in most cases softer EOSs lead to an earlier collapse. The mass-ratio is a secondary effect, but larger q lead to delay collapse. We also showed that in most cases for which a black hole forms the rest mass of the accretion disk increases. In cases of a prompt collapse no massive accretion disk forms.

Gravitational Waves: Varying the mass ratio leads to quantitative changes to the GW frequency, and to qualitative changes of the postmerger spectra. The GW merger frequency is in general largest for equal masses and decreases for increasing q . For MS1b f_{mrg} decreases from 1.45 kHz to 0.09 kHz when q goes from 1 to 1.75 respectively. No significant effect are instead on the post-merger frequency f_2 . We believe the latter is due to the limited accuracy the peak frequency can be extracted, ultimately related to the broad character of the spectra peak. However, we find that for unequal masses the characteristic secondary peaks f_s in the spectrum tend to disappear for large q , and they are actually absent for high mass ratio systems, see Fig. 11.

Our spectrograms highlight the rich structure of the multipolar GW waveform. Modes with azimuthal number $m = 1, 3$, in particular, become progressively more relevant for larger q , although it is unlikely their effect will be observed in next LIGO/Virgo observations, e.g. [84]. Furthermore, for configurations producing a MNS merger remnant, the spectrograms show that the post-merger frequencies increase over time in a chirp-like fashion as the merger remnant becomes more compact. This implies that the postmerger spectrum is in fact continuous and not discrete as anticipated in [68].

The total emitted GW energy is a decreasing function of q during both the inspiral and the post-merger phase. This qualitative behavior is already known from binary black hole systems, but here we extend the result to BNS. This is nontrivial since for BNS tidal interactions play an important role during inspiral-merger and the postmerger phase has different physics from black hole binaries. We find that neutron stars with softer EOS emit more energy. In addition to the total energy, also the mode hierarchy changes by varying q . We find that the energy in the $m = 3$ (and $m = 1$) emission channel increase for larger q and contribute up to 1% to the total emitted energy up to merger.

Electromagnetic counterparts: A GW detection of BNSs will trigger observations to capture follow-up electromagnetic emissions. We used simplified models to estimate the luminosity, peak time, and light curves of macronovae counterparts and the peak time and fluence of radio flares. We showed that the peak luminosity, peak time, and persistency of these counterparts are strongly dependent on the mass ratio q . Unequal mass BNS systems are more luminous in the EM, than equal mass systems because of more massive ejecta. The larger the mass ratio, the more delayed is the luminosity peak. Also our estimated macronova lightcurves are more persistent for larger mass ratios; they could be detected up to a few weeks, see Fig. 18. Similarly to black hole neutron star mergers and differently from $q \sim 1$ BNS, the dynamical ejecta of large q BNS are confined to the equatorial plane and will not obscure optical emissions from the disk wind [94]. Thus, the latter might be detectable for face-on binaries⁵.

Numerical uncertainties have been carefully evaluated on multiple quantities, see Appendix A, and we are confident on the presented results. However, our simulations do not account for microphysics as done in other works e.g. [30–33, 65, 90, 91]. The simplified assumptions in our work have been necessary to simulated a large number of BNS configurations, and in order to better control the numerical errors. We believe our results hold at least at a qualitative level; dedicated simulations of selected

⁵ We thank D.Radice for pointing this out.

configurations that include a more sophisticated treatment of microphysics should be performed in the future to validate our predictions.

Appendix A: Accuracy

Our simulations are pushed in a region of the BNS parameter space, which received little or no attention in the past. Thus, we present some diagnostics for the accuracy of our results considering the initial configurations and the dynamical simulations. However, we refer the reader to [20, 35] for a more detailed discussion about the convergence and accuracy of SGRID and [29, 53, 95] for the accuracy of BAM.

a. Initial configurations

We start with giving the initial linear ADM-momentum and the eccentricity of our configurations in Tab. VII. We have not performed any eccentricity reduction. Thus the final eccentricities lie in a range of 10^{-3} to 10^{-2} . The initial linear momentum of the system (Tab. VII) is in most cases of the order of 10^{-5} to 10^{-4} . For a few cases, those which employ a large mass ratio and use a soft EOS, the linear momentum is rather large. The large linear momentum leads to a movement of the center of mass and therefore results obtained from those systems possess a larger error/uncertainty.

As already explained in [20], it is difficult to construct initial data for very compact stars. In this case the elliptic solver cannot always solve the equation for the conformal factor ψ within the main iteration, because the values from the previous iterations are not good enough as an initial guess for the Newton-Raphson scheme we use. In [20] we could circumvent this issue by skipping the elliptic solve for ψ when this problem occurs. The overall iteration still succeeds if we do not skip this elliptic solve too often. However, for e.g. SLy-100175 this skip occurs so often that we cannot find a good solution for ψ at all. In this case we observe spurious oscillations in ψ near spatial infinity. We were able to cure this problem by changing the boundary condition for ψ . Normally the boundary condition for ψ is simply

$$\lim_{r \rightarrow \infty} \psi = 1. \quad (\text{A1})$$

When we encounter the problems mentioned above we change this condition to

$$\psi = 1 \text{ if } r > 10000M, \quad (\text{A2})$$

so that $\psi = 1$ for all grid points that are further away than $10000M$. We do the same for all other elliptic fields. While this leads to a less accurate boundary conditions, it avoids spurious oscillations in ψ near spatial infinity, and it allows the iteration to succeed. We apply these modified boundary conditions only for configurations where the above mentioned problems occur.

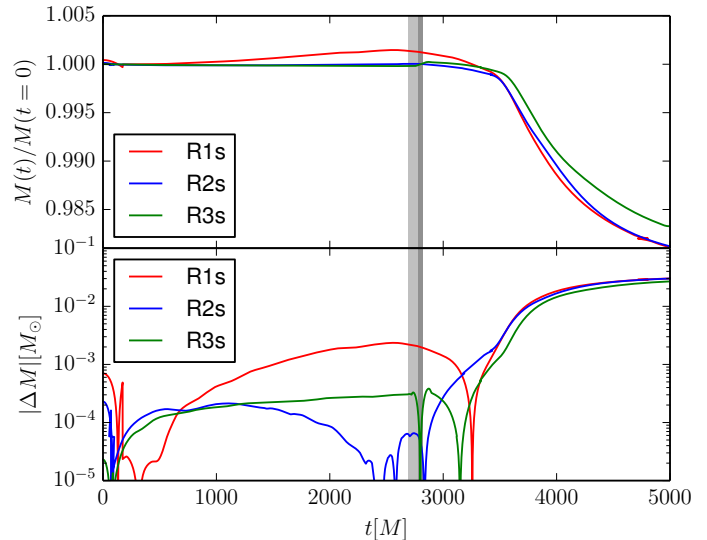


FIG. 20. Mass conservation of MS1b-094194. Top panel shows the mass evolution of the baryonic mass rescaled to its initial value. Bottom panel shows $\Delta M = M(t) - M(t=0)$. We mark the moment of merger as gray shaded regions, where the light gray region marks the interval $[t_{R1s}^{mrg}, t_{R2s}^{mrg}]$, and where the dark shaded region is $[t_{R2s}^{mrg}, t_{R3s}^{mrg}]$. The error in the total mass stays below 0.2% even for the lowest resolution until the time where material leaves the computational domain as ejecta.

b. Mass conservation

We are not only interested in the correctness and accuracy of our initial data, of big importance is the performance during the dynamical evolutions. We present here some diagnostics variables for the most extreme case for which we also have three different resolutions: MS1b-094194. We will start with discussing the mass conservation.

In Ref. [29] it was shown in detail that an additional correction step during the Berger-Oliger [58] or Berger-Collela [61] time stepping improves the mass conservation significantly (up to several orders in some test cases). We do not want to repeat the analysis here and refer the reader to [29, 53] for a detailed discussion. Nevertheless, we want to present mass conservation for at least one of our simulations. Figure 20 shows the mass conservation for MS1b-094194. Clearly visible is that up to the moment of merger mass conservation improves for increasing resolution⁶. Also after the merger no considerable mass loss is present and the difference to the initial mass stays even for the lowest resolution below 0.2%. At later times $\sim 3500M$ material is leaving the computational

⁶ We present the merger as a time interval. Due to different numerical dissipation for different resolutions the merger happens at different times. The light gray area corresponds to the interval $[t_{R1s}^{mrg}, t_{R2s}^{mrg}]$, where the dark region corresponds to $[t_{R2s}^{mrg}, t_{R3s}^{mrg}]$.

TABLE VII. Eccentricity and initial linear momentum of the configurations. Columns: Eccentricity computed from the proper density according to [20] (result stated for the highest resolution and in brackets for the second highest resolution), initial x,y,z-component of the linear momentum measured by SGRID.

Name	$ \hat{e}_d[10^{-3}] $	P_{ADM}^x	P_{ADM}^y	P_{ADM}^z
ALF2-137137	6.8 (6.3)	3.5×10^{-6}	-4.4×10^{-10}	1.8×10^{-9}
H4-137137	13 (13)	-9.5×10^{-7}	-7.4×10^{-11}	3.8×10^{-9}
MS1b-137137	3.9 (3.9)	-1.7×10^{-7}	4.0×10^{-10}	2.0×10^{-9}
SLy-137137	15 (15)	5.8×10^{-8}	-2.3×10^{-10}	1.3×10^{-9}
ALF2-122153	10 (10)	1.2×10^{-6}	-1.9×10^{-4}	5.5×10^{-8}
H4-122153	6.6 (6.7)	-1.9×10^{-7}	6.6×10^{-4}	2.4×10^{-7}
MS1b-122153	8.9 (9.0)	-2.2×10^{-7}	-9.0×10^{-6}	2.5×10^{-6}
SLy-122153	8.2 (8.3)	3.9×10^{-7}	-2.5×10^{-3}	3.3×10^{-8}
ALF2-100150	4.4 (4.8)	-4.3×10^{-6}	2.5×10^{-4}	1.9×10^{-7}
H4-100150	12 (8.9)	-2.5×10^{-8}	1.3×10^{-4}	5.7×10^{-7}
MS1b-100150	16 (16)	9.3×10^{-7}	-4.0×10^{-5}	3.5×10^{-8}
SLy-100150	12 (12)	1.9×10^{-7}	1.7×10^{-4}	-8.6×10^{-8}
ALF2-110165	23 (22)	2.2×10^{-7}	1.6×10^{-4}	-5.9×10^{-8}
H4-110165	3.3 (3.5)	4.2×10^{-7}	-4.9×10^{-4}	1.1×10^{-6}
MS1b-110165	11 (14)	1.2×10^{-6}	1.3×10^{-4}	1.4×10^{-6}
SLy-110165	8.1 (8.3)	-2.1×10^{-6}	1.2×10^{-3}	9.8×10^{-8}
ALF2-117175	3.9 (4.1)	-7.5×10^{-6}	-1.4×10^{-3}	2.5×10^{-8}
H4-117175	3.7 (3.8)	-3.5×10^{-7}	6.7×10^{-7}	9.3×10^{-5}
MS1b-117175	6.2 (6.4)	-1.4×10^{-7}	1.7×10^{-4}	2.6×10^{-8}
SLy-117175	4.1 (4.5)	-1.8×10^{-7}	-4.6×10^{-5}	1.0×10^{-8}
ALF2-100175	1.4 (1.6)	-9.5×10^{-6}	-3.7×10^{-3}	3.5×10^{-6}
H4-100175	4.4 (4.6)	6.6×10^{-7}	1.3×10^{-4}	1.9×10^{-6}
MS1b-100175	8.2 (8.4)	1.6×10^{-7}	3.5×10^{-4}	1.1×10^{-7}
SLy-100175	6.7 (8.2)	-2.5×10^{-7}	3.0×10^{-5}	-6.1×10^{-10}
MS1b-094194	3.4 (3.4)	4.2×10^{-7}	-1.1×10^{-5}	-2.0×10^{-6}

domain where the hydrodynamical variables are evolved and therefore the total baryonic mass is decreasing for all resolutions. This feature is present for most of our simulations using spherical shells. The situation changes for simulations without shells, since the GRHD equations are solved for those simulations also on level $l = 0$.

c. ADM Constraints

Since we use the 3+1 decomposition, see [96, 97] for textbook explanations, we have to ensure that our numerical evolution is a solution to Einstein's field equations, i.e., the Hamiltonian and the momentum constraints have to be zero over the entire simulation. While we explicitly solve the constraints to obtain our initial data, the constraints are not solved during the simulation. Figure 21 shows the L_2 volume norm of the Hamiltonian constraint (top panel) and the L_2 volume norm of the square magnitude of the momentum constraint (bottom panel) during the simulation. We see that due to the constraint damping properties of the Z4c evolution system

the constraints stay at or below the value of the initial data. Oscillations during the inspiral are mostly caused by the interface between the shells and the boxes and the movement of inner refinement levels which follow the motion of the neutron stars. After merger those oscillations are absent since the stars stay near the center or only move with a small velocity compared to the inspiral. During the inspiral an increasing resolution shows the expected convergence, see [53] for a detailed discussion. After the merger the situation is less clear due to the highly nonlinear evolution and the possible formation of shocks.

d. ADM Energy and angular momentum

In principle, the ADM energy and angular momentum have to be conserved for isolated systems. Because we are computing the ADM quantities at a finite distance to the binary system, and energy is emitted via GWs, the ADM quantities do not stay constant. To compensate this fact we compute the amount of radiated energy

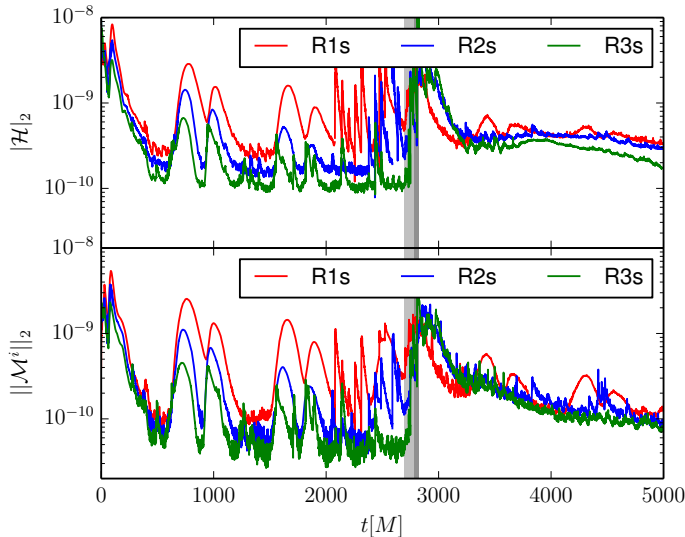


FIG. 21. ADM Constraints for MS1b-094194. Top panel shows the L_2 -volume norm of the Hamiltonian constraint $|\mathcal{H}|_2$. The lower panel shows the square magnitude of the momentum constraint $\|\mathcal{M}^i\|_2 = \sqrt{|\mathcal{M}^x|_2^2 + |\mathcal{M}^y|_2^2 + |\mathcal{M}^z|_2^2}$. The constraints are evaluated on level $l = 1$. The constraints are decreasing for increasing resolution during the inspiral of the neutron stars. For the whole simulation the constraints stay below or at the constraint violation of the initial slice due to the constraint damping of the Z4c scheme. We have filtered our data with an average filter to allow a better visualization and reduce high frequency noise.

and angular momentum and include this in our calculation. Another aspect, not included in our energy/angular momentum budget is material which leaves the computational domain, cf. the discussion about the total baryonic mass. Figure 22 (upper panel) shows the deviation of the ADM-energy from the initial value. Up to the moment of merger the error is $\approx 0.8\%$ for the lowest and $\approx 0.2\%$ for the highest resolution. Figure 22 (bottom panel) visualizes the conservation of the ADM-angular momentum J_{ADM} . In both panels we show as a shaded line the actual numerical data and as a solid line the result after applying an averaging filter to oscillations caused by the motion of the two NSs. However, we find overall errors below 1% even for the lowest resolution. For higher resolutions the error goes down to $\approx 0.2\%$.

e. Waveforms

Although we have investigated the convergence behavior of BAM waveforms many times in the past [45, 53, 95], we present here a convergence test for the waveform of MS1b-094194. The reason is that this configuration has new features with respect previous equal-masses runs, including new initial data, the large mass-ratio, the significant mass transfer at low resolutions. Overall we find that the numerical computation is more challenging and

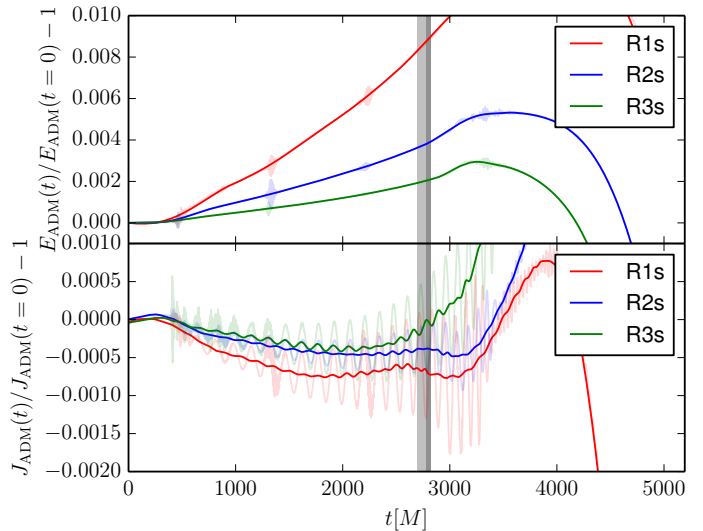


FIG. 22. ADM quantities for MS1b-094194. Top panel shows the ADM energy, which we correct with the amount of GW energy emitted by the system. The quantity is conserved at or below the 0.5% level for R2s and R3s until material is leaving the computational domain. Bottom panel shows the ADM-angular momentum corrected by the amount of angular momentum extracted via GW emission. For R2s and R3s the ADM-angular momentum is conserved better than 0.05%. In both panels we show the numerical data as semi-transparent lines and the results after applying an average filter as solid lines. This filtering reduces oscillations caused by the orbital motion and allows an easier interpretation of the data.

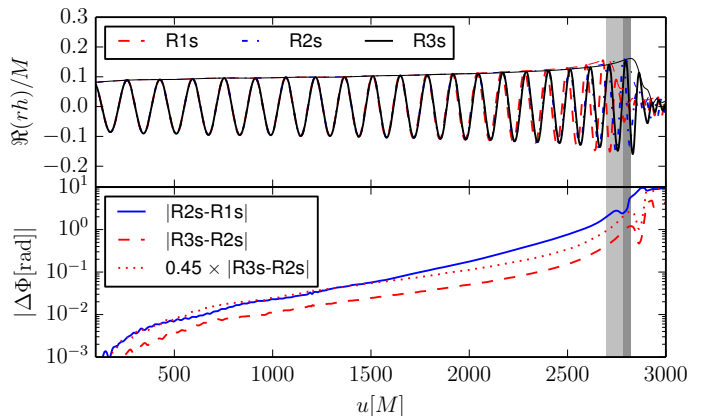


FIG. 23. Top panel: Real part of the dominant (2,2) GW mode of MS1b-094194. Bottom panel: Phase difference between different resolutions. The dotted red line corresponds to a convergence order of 1.3. As for the previous discussions the different moments of merger are represented as a shaded region.

higher resolutions would be required to achieve the same accuracy of $q \sim 1$ runs.

Figure 23 (upper panel) shows the real part and the amplitude of the dominant (2,2) mode for MS1b-094194 for three different resolutions. Up to $\sim 1600M$ we find a convergence order ≈ 1.3 , cf. red dotted line in bottom

panel of Fig. 23. The bottom panel of Fig. 23 also present the difference between R2s and R1s as a dashed red line and the difference between R3s and R2s as a solid blue line. The convergence order seems to increase during the end of the simulation ($t > 1800M$) and overconvergence is present, cf. [53, 98, 99]. Beside the resolutions employed, this might be also caused by the mass transfer which is much stronger for the R1s simulation than for the higher resolved simulations.

ACKNOWLEDGMENTS

It is a pleasure to thank Roland Haas, Ian Hinder, Tanja Hinderer, Nathan K. Johnson-McDaniel, Charalampos M. Markakis, Serguei Ossokine, Justin Vines for helpful discussions and Casey Handmer and David Radice for comments on the manuscript. We are very grateful to Kyohei Kawaguchi for discussions about the ejecta during BHNS mergers and for making his model and code publicly available [75]. Computations were performed on SuperMUC at the LRZ (Munich) under the project numbers pr87nu and pr48pu, Juropa/Jureca (Jülich) under the project number HJN26 and HPO21, Stampede (Texas, XSEDE allocation - TG-PHY140019), and the Jena group local cluster `quadler`.

-
- [1] B. P. Abbott et al. (Virgo, LIGO Scientific), *Phys. Rev. Lett.* **116**, 061102 (2016), 1602.03837.
 - [2] B. Abbott et al. (Virgo, LIGO Scientific), *Phys. Rev. Lett.* **116**, 241103 (2016), 1606.04855.
 - [3] W. Del Pozzo, T. G. F. Li, M. Agathos, C. V. D. Broeck, and S. Vitale, *Phys. Rev. Lett.* **111**, 071101 (2013), 1307.8338.
 - [4] S. Rosswog, *Int.J.Mod.Phys.* **D24**, 1530012 (2015), 1501.02081.
 - [5] R. Fernandez and B. D. Metzger, *Ann. Rev. Nucl. Part. Sci.* **66**, 2115 (2016), 1512.05435.
 - [6] N. Tanvir, A. Levan, A. Fruchter, J. Hjorth, K. Wiersema, et al., *Nature* **500**, 547 (2013), 1306.4971.
 - [7] B. Paczynski, *Astrophys. J.* **308**, L43 (1986).
 - [8] D. Eichler, M. Livio, T. Piran, and D. N. Schramm, *Nature* **340**, 126 (1989).
 - [9] A. M. Soderberg et al., *Astrophys. J.* **650**, 261 (2006), astro-ph/0601455.
 - [10] E. Nakar and T. Piran, *Nature* **478**, 82 (2011), 1102.1020.
 - [11] M. L. Rawls, J. A. Orosz, J. E. McClintock, M. A. P. Torres, C. D. Bailyn, and M. M. Buxton, *Astrophys. J.* **730**, 25 (2011), 1101.2465.
 - [12] F. Ozel, D. Psaltis, R. Narayan, and A. S. Villarreal, *Astrophys. J.* **757**, 55 (2012), 1201.1006.
 - [13] P. Demorest, T. Pennucci, S. Ransom, M. Roberts, and J. Hessels, *Nature* **467**, 1081 (2010), 1010.5788.
 - [14] J. Antoniadis, P. C. Freire, N. Wex, T. M. Tauris, R. S. Lynch, et al., *Science* **340**, 6131 (2013), 1304.6875.
 - [15] S. Lawrence, J. G. Tervala, P. F. Bedaque, and M. C. Miller, *Astrophys. J.* **808**, 186 (2015), 1505.00231.
 - [16] J. M. Lattimer, *Ann. Rev. Nucl. Part. Sci.* **62**, 485 (2012), 1305.3510.
 - [17] J. K. Swiggum et al., *Astrophys. J.* **805**, 156 (2015), 1503.06276.
 - [18] J. G. Martinez, K. Stovall, P. C. C. Freire, J. S. Deneva, F. A. Jenet, M. A. McLaughlin, M. Bagchi, S. D. Bates, and A. Ridolfi, *Astrophys. J.* **812**, 143 (2015), 1509.08805.
 - [19] M. Dominik, K. Belczynski, C. Fryer, D. E. Holz, E. Berti, T. Bulik, I. Mandel, and R. O’Shaughnessy, *Astrophys. J.* **759**, 52 (2012), 1202.4901.
 - [20] T. Dietrich, N. Moldenhauer, N. K. Johnson-McDaniel, S. Bernuzzi, C. M. Markakis, B. Brügmann, and W. Tichy, *Phys. Rev. D* **91**, 124007 (2015), 1507.07100.
 - [21] M. Burgay, N. D’Amico, A. Possenti, R. Manchester, A. Lyne, et al., *Nature* **426**, 531 (2003), astro-ph/0312071.
 - [22] R. S. Lynch, P. C. C. Freire, S. M. Ransom, and B. A. Jacoby, *Astrophys. J.* **745**, 109 (2012), 1112.2612.
 - [23] M. C. Miller and J. M. Miller, *Phys. Rept.* **548**, 1 (2014), 1408.4145.
 - [24] T. Dietrich et al., In preparation (2016).
 - [25] M. Shibata, K. Taniguchi, and K. Uryu, *Phys. Rev.* **D68**, 084020 (2003), gr-qc/0310030.
 - [26] L. Rezzolla, L. Baiotti, B. Giacomazzo, D. Link, and J. A. Font, *Class. Quant. Grav.* **27**, 114105 (2010), 1001.3074.
 - [27] K. Hotokezaka, K. Kiuchi, K. Kyutoku, H. Okawa, Y.-i. Sekiguchi, et al., *Phys.Rev.* **D87**, 024001 (2013), 1212.0905.
 - [28] A. Bauswein, S. Goriely, and H.-T. Janka, *Astrophys.J.* **773**, 78 (2013), 1302.6530.
 - [29] T. Dietrich, S. Bernuzzi, M. Ujevic, and B. Brügmann, *Phys. Rev.* **D91**, 124041 (2015), 1504.01266.
 - [30] S. Bernuzzi, D. Radice, C. D. Ott, L. F. Roberts, P. Moesta, and F. Galeazzi, *Phys. Rev.* **D94**, 024023 (2016), 1512.06397.
 - [31] L. Lehner, S. L. Liebling, C. Palenzuela, and P. Motl (2016), 1605.02369.
 - [32] L. Lehner, S. L. Liebling, C. Palenzuela, O. L. Caballero, E. O’Connor, M. Anderson, and D. Neilsen (2016), 1603.00501.
 - [33] Y. Sekiguchi, K. Kiuchi, K. Kyutoku, M. Shibata, and K. Taniguchi, *Phys. Rev.* **D93**, 124046 (2016), 1603.01918.
 - [34] W. Tichy, *Phys.Rev.* **D74**, 084005 (2006), gr-qc/0609087.
 - [35] W. Tichy, *Class.Quant.Grav.* **26**, 175018 (2009), 0908.0620.
 - [36] W. Tichy, *Phys.Rev.* **D80**, 104034 (2009), 0911.0973.
 - [37] J. Wilson and G. Mathews, *Phys.Rev.Lett.* **75**, 4161 (1995).
 - [38] J. Wilson, G. Mathews, and P. Marronetti, *Phys.Rev.* **D54**, 1317 (1996), gr-qc/9601017.
 - [39] J. York, James W., *Phys.Rev.Lett.* **82**, 1350 (1999), gr-qc/9810051.
 - [40] W. Tichy, *Phys.Rev.* **D84**, 024041 (2011), 1107.1440.

- [41] W. Tichy, Phys. Rev. D **86**, 064024 (2012), 1209.5336.
- [42] B. Brügmann, J. A. Gonzalez, M. Hannam, S. Husa, U. Sperhake, et al., Phys.Rev. **D77**, 024027 (2008), gr-qc/0610128.
- [43] M. Thierfelder, S. Bernuzzi, and B. Brügmann, Phys.Rev. **D84**, 044012 (2011), 1104.4751.
- [44] S. Bernuzzi and D. Hilditch, Phys. Rev. **D81**, 084003 (2010), 0912.2920.
- [45] D. Hilditch, S. Bernuzzi, M. Thierfelder, Z. Cao, W. Tichy, et al., Phys. Rev. **D88**, 084057 (2013), 1212.2901.
- [46] C. Bona, J. Massó, J. Stela, and E. Seidel, in *The Seventh Marcel Grossmann Meeting: On Recent Developments in Theoretical and Experimental General Relativity, Gravitation, and Relativistic Field Theories*, edited by R. T. Jantzen, G. M. Keiser, and R. Ruffini (World Scientific, Singapore, 1996).
- [47] M. Alcubierre, B. Brügmann, P. Diener, M. Koppitz, D. Pollney, et al., Phys.Rev. **D67**, 084023 (2003), gr-qc/0206072.
- [48] J. R. van Meter, J. G. Baker, M. Koppitz, and D.-I. Choi, Phys. Rev. **D73**, 124011 (2006), gr-qc/0605030.
- [49] J. S. Read, B. D. Lackey, B. J. Owen, and J. L. Friedman, Phys. Rev. **D79**, 124032 (2009), 0812.2163.
- [50] M. Shibata, K. Taniguchi, and K. Uryu, Phys. Rev. **D71**, 084021 (2005), gr-qc/0503119.
- [51] A. Bauswein, H.-T. Janka, and R. Oechslin, Phys.Rev. **D82**, 084043 (2010), 1006.3315.
- [52] R. Borges, M. Carmona, B. Costa, and W. S. Don, Journal of Computational Physics **227**, 3191 (2008).
- [53] S. Bernuzzi and T. Dietrich (2016), 1604.07999.
- [54] C. Ronchi, R. Iacono, and P. Paolucci, Journal of Computational Physics **124**, 93 (1996), ISSN 0021-9991, URL <http://www.sciencedirect.com/science/article/pii/S0021999196900479>.
- [55] J. Thornburg, Class. Quant. Grav. **21**, 3665 (2004), gr-qc/0404059.
- [56] D. Pollney, C. Reisswig, E. Schnetter, N. Dorband, and P. Diener, Phys. Rev. **D83**, 044045 (2011), 0910.3803.
- [57] M. Ruiz, D. Hilditch, and S. Bernuzzi, Phys. Rev. **D83**, 024025 (2011), 1010.0523.
- [58] M. J. Berger and J. Olinger, J.Comput.Phys. **53**, 484 (1984).
- [59] T. Dietrich and S. Bernuzzi, Phys.Rev. **D91**, 044039 (2015), 1412.5499.
- [60] W. E. East, F. Pretorius, and B. C. Stephens, Phys.Rev. **D85**, 124010 (2012), 1112.3094.
- [61] M. J. Berger and P. Colella, Journal of Computational Physics **82**, 64 (1989).
- [62] T. W. Baumgarte, S. L. Shapiro, and M. Shibata, Astrophys. J. **528**, L29 (2000), astro-ph/9910565.
- [63] W. E. East and F. Pretorius, Astrophys.J. **760**, L4 (2012), 1208.5279.
- [64] W. Kastaun and F. Galeazzi, Phys.Rev. **D91**, 064027 (2015), 1411.7975.
- [65] D. Radice, F. Galeazzi, J. Lippuner, L. F. Roberts, C. D. Ott, and L. Rezzolla (2016), 1601.02426.
- [66] T. Damour and A. Nagar, Phys. Rev. **D80**, 084035 (2009), 0906.0096.
- [67] S. Bernuzzi, A. Nagar, S. Balmelli, T. Dietrich, and M. Ujevic, Phys.Rev.Lett. **112**, 201101 (2014), 1402.6244.
- [68] S. Bernuzzi, T. Dietrich, and A. Nagar, Phys. Rev. Lett. **115**, 091101 (2015), 1504.01764.
- [69] S. Bernuzzi, A. Nagar, M. Thierfelder, and B. Brügmann, Phys.Rev. **D86**, 044030 (2012), 1205.3403.
- [70] S. Bernuzzi, A. Nagar, T. Dietrich, and T. Damour, Phys.Rev.Lett. **114**, 161103 (2015), 1412.4553.
- [71] T. Hinderer, A. Taracchini, F. Foucart, A. Buonanno, J. Steinhoff, M. Duez, L. E. Kidder, H. P. Pfeiffer, M. A. Scheel, B. Szilagy, et al. (2016), 1602.00599.
- [72] K. Hotokezaka, K. Kyutoku, H. Okawa, and M. Shibata, Phys. Rev. **D91**, 064060 (2015), 1502.03457.
- [73] Y. Sekiguchi, K. Kiuchi, K. Kyutoku, and M. Shibata, Phys.Rev. **D91**, 064059 (2015), 1502.06660.
- [74] F. Foucart, Phys. Rev. **D86**, 124007 (2012), 1207.6304.
- [75] K. Kawaguchi, K. Kyutoku, M. Shibata, and M. Tanaka (2016), 1601.07711.
- [76] S. Bernuzzi, T. Dietrich, W. Tichy, and B. Brügmann, Phys. Rev. **D89**, 104021 (2014), 1311.4443.
- [77] M. Shibata and K. Taniguchi, Phys.Rev. **D73**, 064027 (2006), astro-ph/0603145.
- [78] C. Reisswig and D. Pollney, Class.Quant.Grav. **28**, 195015 (2011), 1006.1632.
- [79] J. A. Clark, A. Bauswein, N. Stergioulas, and D. Shoemaker, Class. Quant. Grav. **33**, 085003 (2016), 1509.08522.
- [80] F. Foucart, R. Haas, M. D. Duez, E. O'Connor, C. D. Ott, L. Roberts, L. E. Kidder, J. Lippuner, H. P. Pfeiffer, and M. A. Scheel, Phys. Rev. **D93**, 044019 (2016), 1510.06398.
- [81] L. Rezzolla and K. Takami (2016), 1604.00246.
- [82] K. Takami, L. Rezzolla, and L. Baiotti, Phys.Rev. **D91**, 064001 (2015), 1412.3240.
- [83] A. Bauswein and N. Stergioulas, Phys. Rev. **D91**, 124056 (2015), 1502.03176.
- [84] D. Radice, S. Bernuzzi, and C. D. Ott (2016), 1603.05726.
- [85] T. Damour, A. Nagar, and S. Bernuzzi, Phys.Rev. **D87**, 084035 (2013), 1212.4357.
- [86] E. Barausse, V. Morozova, and L. Rezzolla (2012), 1206.3803.
- [87] L. Blanchet, Living Rev. Relativity **17**, 2 (2014), 1310.1528.
- [88] V. Paschalidis, W. E. East, F. Pretorius, and S. L. Shapiro, Phys. Rev. **D92**, 121502 (2015), 1510.03432.
- [89] D. Grossman, O. Korobkin, S. Rosswog, and T. Piran, Mon. Not. Roy. Astron. Soc. **439**, 757 (2014), 1307.2943.
- [90] C. Palenzuela, S. L. Liebling, D. Neilsen, L. Lehner, O. L. Caballero, E. O'Connor, and M. Anderson, Phys. Rev. D **92**, 044045 (2015), 1505.01607.
- [91] O. Just, A. Bauswein, R. A. Pulpillo, S. Goriely, and H. T. Janka, Mon. Not. Roy. Astron. Soc. **448**, 541 (2015), 1406.2687.
- [92] S. Wanajo, Y. Sekiguchi, N. Nishimura, K. Kiuchi, K. Kyutoku, and M. Shibata, Astrophys. J. **789**, L39 (2014), 1402.7317.
- [93] Webpage Karaguchi, URL http://www2.yukawa.kyoto-u.ac.jp/~kyohei.kawaguchi/kn_calc/main.html.
- [94] D. Kasen, R. Fernandez, and B. Metzger, Mon. Not. Roy. Astron. Soc. **450**, 1777 (2015), 1411.3726.
- [95] S. Bernuzzi, M. Thierfelder, and B. Brügmann, Phys.Rev. **D85**, 104030 (2012), 1109.3611.
- [96] M. Alcubierre, *Introduction to 3+1 Numerical Relativity* (Oxford University Press, 2008).
- [97] T. W. Baumgarte and S. L. Shapiro, *Numerical Relativity: Solving Einstein's Equations on the Computer* (Cambridge University Press, New York, 2010).

- [98] D. Radice, L. Rezzolla, and F. Galeazzi, *Class.Quant.Grav.* **31**, 075012 (2014), 1312.5004.
- [99] D. Radice, L. Rezzolla, and F. Galeazzi (2015), 1502.00551.